





Article

Nature-Derived Compounds as Potential Bioactive Leads against CDK9-Induced Cancer: Computational and Network Pharmacology Approaches

Abu Saim Mohammad Saikat ¹, Khattab Al-Khafaji ², Hafeza Akter ³, Jong-Gu Choi ³, Mahbub Hasan ^{1,3,*} and Sang-Suk Lee ^{3,*}

¹ Department of Biochemistry and Molecular Biology, Life Science Faculty, Bangabandhu Sheikh Mujibur Rahman Science and Technology University, Gopalganj 8100, Bangladesh

² College of Dentistry, The University of Mashreq, Baghdad 10022, Iraq

³ Department of Oriental Biomedical Engineering, Sangji University, Wonju 26339, Republic of Korea

* Correspondence: mahbub.bmb@gmail.com (M.H.); sslee@sangji.ac.kr (S.-S.L.)

Abstract: Given the importance of cyclin-dependent kinases (CDKs) in the maintenance of cell development, gene transcription, and other essential biological operations, CDK blockers have been generated to manage a variety of disorders resulting from CDK irregularities. Furthermore, CDK9 has a crucial role in transcription by regulating short-lived anti-apoptotic genes necessary for cancer cell persistence. Addressing CDK9 with blockers has consequently emerged as a promising treatment for cancer. This study scrutinizes the effectiveness of nature-derived compounds (geniposidic acid, quercetin, geniposide, curcumin, and withanolide C) against CDK9 through computational approaches. A molecular docking study was performed after preparing the protein and the ligands. The selected blockers of the CDK9 exerted reliable binding affinities (−8.114 kcal/mol to −13.908 kcal/mol) against the selected protein, resulting in promising candidates compared to the co-crystallized ligand (LCI). The binding affinity of geniposidic acid (−13.908 kcal/mol) to CDK9 is higher than quercetin (−10.775 kcal/mol), geniposide (−9.969 kcal/mol), curcumin (−9.898 kcal/mol), withanolide C (−8.114 kcal/mol), and the co-crystallized ligand LCI (−11.425 kcal/mol). Therefore, geniposidic acid is a promising inhibitor of CDK9. Moreover, the molecular dynamics studies assessed the structure–function relationships and protein–ligand interactions. The network pharmacology study for the selected ligands demonstrated the auspicious compound–target–pathway signaling pathways vital in developing tumor, tumor cell growth, differentiation, and promoting tumor cell progression. Moreover, this study concluded by analyzing the computational approaches the natural-derived compounds that have potential interacting activities against CDK9 and, therefore, can be considered promising candidates for CDK9-induced cancer. To substantiate this study's outcomes, in vivo research is recommended.

Keywords: CDK9; molecular docking; molecular dynamics; network pharmacology; PPI network; free energy landscape; CDK9-induced cancer



Citation: Saikat, A.S.M.; Al-Khafaji, K.; Akter, H.; Choi, J.-G.; Hasan, M.; Lee, S.-S. Nature-Derived Compounds as Potential Bioactive Leads against CDK9-Induced Cancer: Computational and Network Pharmacology Approaches. *Processes* **2022**, *10*, 2512. <https://doi.org/10.3390/pr10122512>

Academic Editors: Alina Pyka-Pajak and Roberto Pisano

Received: 14 September 2022

Accepted: 23 November 2022

Published: 25 November 2022

Publisher's Note: MDPI stays neutral with regard to jurisdictional claims in published maps and institutional affiliations.



Copyright: © 2022 by the authors. Licensee MDPI, Basel, Switzerland. This article is an open access article distributed under the terms and conditions of the Creative Commons Attribution (CC BY) license (<https://creativecommons.org/licenses/by/4.0/>).

1. Introduction

The division of cells is one of the essential biological operations, engaging in many physiological mechanisms, including individual development, tissue regeneration, organ homeostasis, and the malignant action of cancer. The series of steps in cell division is called the cell cycle, and it consists of a synthesis phase, a mitotic segregation process, and two intervening phases, G1 and G2 [1–3]. Mammalian cells expand during the G1 phase in preparation for DNA synthesis, governed by a “restriction point”. Intrinsic variables (such as protein production) and extracellular factors (such as environmental conditions) affect whether a cell can begin the cell cycle (such as growth factors (GFs)). In the lack of these crucial components, the cell ceases its cell cycle and enters the G0 phase

of dormancy. Three “checkpoints” are involved in regulating the cell cycle: the G1/S, G2/M, and mitotic spindle checkpoints [4–7]. The eukaryotic cell cycle is governed by a standard core process, incorporating cyclin-dependent kinases (CDKs), which increase DNA synthesis and chromosome segregation by phosphorylating their substrate [8–10].

In addition to directing the cell cycle, several CDKs, including CDK9, have contributed to transcriptional regulation. CDK9 can phosphorylate RNA polymerase II to enhance transcription extension [11,12]. CDK9 controls the transcription of multiple genes, notably *Myc*, a proto-oncogene that governs mechanisms essential for cell cycle progression and cell development, and *Mcl-1*, an anti-apoptotic representative of the Bcl-2 family that promotes cell survival. Consequently, CDK9 suppression lowers messenger RNA (mRNA) transcription and impedes the expression of target genes (such as *Mcl-1* and *Myc*), which collectively govern cancer cell multiplication and lifespan [13–15]. Conversely, recent influential investigations have demonstrated that CDK9 is involved in gene suppression [16,17]. CDK9 is a legitimate therapeutic target candidate in cancer because it promotes cell proliferation and regulates anti-apoptotic proteins, including *Mcl-1* and *Myc*, that trigger cancer cell longevity. A dysfunctional CDK9-related process has been identified as a critical factor in the development and advancement of lymphomas, breast cancer, prostate cancer, and other malignancies [18–24]. Multiple investigations have demonstrated that aberrant CDK9 signaling is linked to the etiology of many hematological cancers [20,24,25]. Human cells with enhanced *Mcl-1* expression have been connected to the progression of acute myeloid leukemia. Several pathological disorders, including lymphomas and Hodgkin’s disease, have exhibited elevated p-TEFb activity [26,27]. CDK9 is essential to prostate cancer [19]. Primarily, androgens promote the development and lifespan of prostate cells, and most castration-sensitive prostate cancer is responsive to androgen deprivation.

Nevertheless, 20% of prostate cancer patients acquire castrate-resistant prostate cancer (CRPC), which is refractory to standard treatment and is linked with a poor prognosis. By influencing the androgen receptor’s function, CDK9 has subsequently been discovered as a crucial component in CRPC [19,20,28]. Through its involvement with proto-oncogenes, aberrant CDK9 expression is one molecular mechanism in the formation of breast cancer, despite the disease’s heterogeneous genetic background [29]. MiR-874 inhibits proliferation and induces apoptosis and cell cycle arrest, hence playing a crucial role in breast cancer, according to a study. This work identified CDK9 as a specific candidate of miR-874, which affects its protein levels adversely [30]. Furthermore, according to a study, CDK9 inhibits the expression of the proto-oncogene *Myb* in estrogen receptor-positive breast cancer. Using CDK9 blockers such as SNS-032, CDKi, and CAN-508, the role of CDK9 was underlined in this work. These findings revealed an enhancement in tumor cell apoptosis and inhibition of cell proliferation [31].

Several chemical motifs have been designed since CDK9 suppression was recognized as a viable therapeutic option in cancer. As a result, this has been a forthright approach for substantial pharmaceutical firms. These blockers are often ATP-competitive inhibitors with a reduced molecular weight with drug-like characteristics. These compounds are now being tested in clinical studies as anti-proliferative medicines to manage various forms of cancer [25,32–40]. Computer-aided drug discovery is *in silico* pharmacology [41,42]. Modeling and simulation are included in this approach in the broadest sense to learn about the mechanism of action of medications and their toxicity, side effects, and the related pharmacokinetic activities when they engage with a biological process [43–45]. More recently, the biological components of *in silico* screening have been expanded. Therefore, novel integrative approaches can assess the pharmacological profile of compounds on numerous targets [46,47].

Direct cytotoxicity tests on cancer cells of geniposidic acid and geniposide and genipin are frequently used in conjunction with apoptosis assays to demonstrate the promising anti-cancer properties of natural compounds *in vitro* [48–50]. It is effective against a wide range of cancer cells, such as pancreatic adenocarcinoma cells, colorectal cancer, human gastric carcinoma cells, prostate cancer cells, non-small-cell lung cancer cells, breast cancer

cells, hepatocarcinoma cells, human leukemia cells, and tongue squamous carcinoma cells [48,51–58]. Quercetin, a bioactive flavonoid, has drawn the interest of nutritionists and medicinal chemists because of its many health-enhancing properties. It is an excellent antioxidant that has been shown to significantly impact the prevention and treatment of various human malignancies [59–62]. Quercetin's proapoptotic properties can be directly applied to tumor cells, slowing or stopping the progression of a wide range of human malignancies. Multiple in vitro and in vivo investigations using a variety of cell lines and animal models have shown Quercetin's anti-cancer properties [63–67].

On the other hand, Quercetin has a powerful toxic impact on cancer cells while causing minimal or no damage to normal cells [63,68–71]. As an antioxidant, anti-cancer drug, and anti-inflammatory, curcumin has garnered considerable attention during the past couple of decades [72–74]. The synopsis of curcumin's medicinal chemistry and pharmacological investigations regarding anti-cancer efficacy, their principal modes of action, and cellular targets are based on curcumin's experimental and clinical assessment in animal models, cancer cell lines, and humans [75–79]. In addition, the most recent developments in drug delivery methods for curcumin administration to cancer cells have been emphasized [80–84]. Some withanolides, notably the family of steroidal lactones, have anti-cancer properties. However, this is seldom documented for withanolide C, precisely its breast-cancer-fighting properties [85–87]. The investigations intend to assess the capacity of withanolide C to inhibit the growth of breast cancer cells, taking into account the duration and concentration of WHC administration. Withanolide C generated more antiproliferation in malignant breast cancer cell lines than in regular breast cell lines, as measured by ATP depletion [85,88–91]. This investigation aspires to dissect the effectiveness of nature-derived compounds against CDK9 through computational strategies such as geniposidic acid, quercetin, geniposide, curcumin, and withanolide C.

2. Materials and Methods

2.1. Protein Preparation

The crystal architecture of the target protein CDK9/cyclinT1 (PDB id: 6GZH) with the inhibitor-confined complex was received from the protein data bank [92]. The Protein Preparation Wizard (PPW) program of the Maestro v.11.2 (Maestro, Schrödinger, Inc., New York, NY, USA) was executed for protein preparation. The obtained protein was prepared using the Maestro (v.11.2) program's Protein Preparation Wizard (PPW) tool [93]. The PPW program consists of three-step stratagems, including 'Import and Refine', 'Review and Modify', and 'Optimized and Minimize'. In the initial precedent, the protein (PDB id: 6GZH) was pre-processed by adjoining hydrogen atoms, eradicating displeased water molecules outlying 5 Å from the hetero-group and creating het-states performing Epik at pH 7.0 (\pm 2.0). The PPW followed three basic steps: 'Import and Refine', 'Review and Modify', and 'Optimized and Minimize' to prepare the selected protein. First, the PPW organized the protein by connecting hydrogen atoms, obliterating disgruntled water molecules outlying 5 Å from the hetero-group, and assembling het states accomplishing the Epik program at pH 7.0 (\pm 2.0) [94]. Next, the protein was minimized following the RMSD of 0.30 Å applying the OPLS3e force fields [95].

2.2. Ligand Preparation

The ligands, LCI, geniposidic acid, quercetin, geniposide, curcumin, and withanolide C (PubChem CID: 134812748, 443354, 969516, 5280343, 107848, and 101559583, respectively) were collected from the PubChem database [96]. The LigPrep tool (LigPrep, Schrödinger Inc., New York, NY, USA) was employed to transform the ligand structures into three-dimensional arrangements and deliver reliable conformers and tautomers. The LigPrep implement was conducted at unbiased ionization and the OPLS3e force field for underestimating the ligands [95].

2.3. Molecular Docking

The Maestro (v.11.2) GLIDE program was used for all docking studies, resulting in the observation of constructive associations between the ligand and protein [97]. The program Receptor Grid Generation (RGG) was utilized to construct a grid at the position of a co-crystallized ligand. This grid provides the features of the aim protein and the implemented curvature for a more comprehensive ligand posture assessment. The Extra Precision (XP) docking technique was applied during the protein–ligand docking approach [97].

2.4. Analyzing the ADMET Properties of the Selected Ligands

Advancement for the integrity assurance of pharmaceuticals, investigators use *in silico* algorithms to anticipate the absorption, distribution, metabolism, excretion, and toxicity (ADMET) properties of ligands and their defects [98,99]. The SwissADME [100] and the pkCSM [101] programs were used for anticipating the ADMET properties.

2.5. Molecular Dynamics

Implementing the molecular dynamics simulations using Gromacs 2018-3 with GPU acceleration on Ubuntu 18.04 windows subsystem Linux 2 (WSL2) has been carried out regarding the top five docking score compounds and apo form [102]. We selected Charm 27 for all atoms as a forcefield on the determination of ligands' stabilities inside the binding site. The protein–ligand systems were immersed in a TIP3P water box [103]. To maintain the physiological conditions of protein–ligand systems, we added 0.1 M of NaCl. The minimum distance between the box boundary and the protein–ligand complex atoms was 1 (one) nm. SwissParam was utilized to optimize the charge of ligands and generate the files needed for the parameterization of molecular dynamics. The energy of solute–solvent boxes was minimized through the steepest descent algorithm with a maximum force (F_{\max}) of 1000 kJ/mol.nm. The two sequential canonical NVT ensembles and isobaric NPT ensembles were adopted to equilibrate the main protease's apo and holo forms for 100 ps. During equilibrations, systems were coupled with the Parrinello–Rahman pressure and the Berendsen temperature controllers [104] to conserve the pressure 1 bar and the temperature 300 K, respectively. The Particle Mesh Ewald (PME) [105] was appointed to deal with the long range of Coulomb interactions through a Fourier grid spacing of 0.12 nm. In contrast, the short-range van der Waals interactions were calibrated through the Lennard-Jones potential with a cut-off distance of 1 nm. Moreover, the linear constraint solver (LINCS) method [106] was adopted to compel all bond lengths. Finally, they submitted 100 ns of MD simulations. GROMACS tools were used to analyze RMSD, RMSF, RG, SASA, PCA, G_sham, and hydrogen bonding of the obtained trajectories.

2.6. Network-Pharmacology-Based Mechanism Analyses

The predicted targets of LCI, geniposidic acid, quercetin, geniposide, curcumin, and withanolide C were obtained from a Swiss Target Prediction [107] and DIGEP-Pred [108]. The SMILE format of mentioned compounds was uploaded into Swiss Target Prediction and DIGEP-Pred, and the obtained data were downloaded. The protein–protein interaction network database (STRING v.11.0) [109] was used to establish the protein–protein interaction network. The maximal clique centrality (MMC) algorithm in the CytoHubba plug-in for Cytoscape (v.3.8.3) [110] was used for a comprehensive analysis of network topology to obtain the top 41 hub genes. Additionally, the network was analyzed by MCODE, a cluster analysis plug-in for Cytoscape (v.3.8.3) [110], which was utilized to analyze the PPI network [110,111]. Furthermore, the hub genes were subjected to the DAVID database to analyze KEGG pathways. It has been determined that the KEGG pathway has statistically significant and necessary functional mechanisms such as p -value ≤ 0.05 . The ggplot2 was used to visualize the bubble plot, a package provided in the R programming language.

2.7. Construction of the Compound–Target–Pathway Network

In this network, the nodes contain paths, associated core destinations, and prominent links with different shapes and colors. The topological parameters of the node degree in the network were also analyzed using a network analyzer. Then, core connections and corresponding common goals were obtained through the network.

3. Results

3.1. Protein Preparation

The PPW program was used to prepare the protein for the molecular docking investigation. The Ramachandran plot calculation wizard of the PPW program was performed to analyze the Ramachandran plot of the minimized protein. The Ramachandran plot depicts the statistical prevalence of the backbone dihedral angle (ϕ and ψ angles) combinations [112]. Theoretically, the Ramachandran plot has permitted areas to indicate an amino acid's range of potential Phi/Psi angles. In practice, the pattern of observed Phi/Psi frequencies in a protein structure can be used to validate the structure. The Ramachandran plot demonstrated that most proteins were in the favored region (red-colored) and acceptable (yellow-colored) regions. A few amino acid residues, including VAL190, GLY218, GLY161, and GLY28, were found in the unfavored area in the Ramachandran plot (Figure 1).

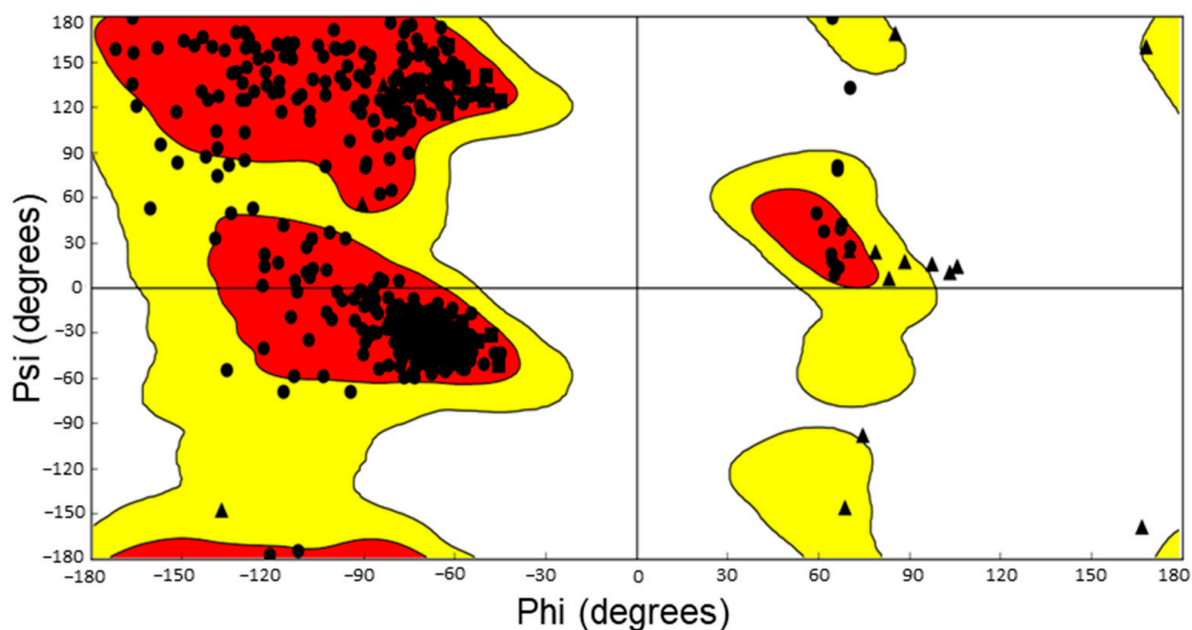


Figure 1. Ramachandran plot of the minimized protein. The ‘red color’, ‘yellow color’, and ‘white color’ regions represent the favored, acceptable, and unfavored regions, respectively. A few amino acids, including VAL190, GLY218, GLY161, and GLY28, are present in the unfavored region.

3.2. Ligand Preparation

The chemical structures of geniposidic acid, quercetin, geniposide, curcumin, withanolide C, and LCI were obtained from the PubChem database in .sdf formats. Moreover, the canonical SMILES and the isomeric SMILES were stored for drawing the chemical structures. Five promising ligands (geniposidic acid, quercetin, geniposide, curcumin, and withanolide C), along with the co-crystallized ligand (LCI), were employed to transform into three-dimensional configuration and generate possible conformers and tautomers (Figure 2). The LigPrep tool was executed at neutral ionization and the OPLS3e force field for minimizing the ligands. The LigPrep tool minimized the ligands for performing docking with the protein 6GZH. The prepared ligands were stored for performing molecular docking simulation with the selected protein.

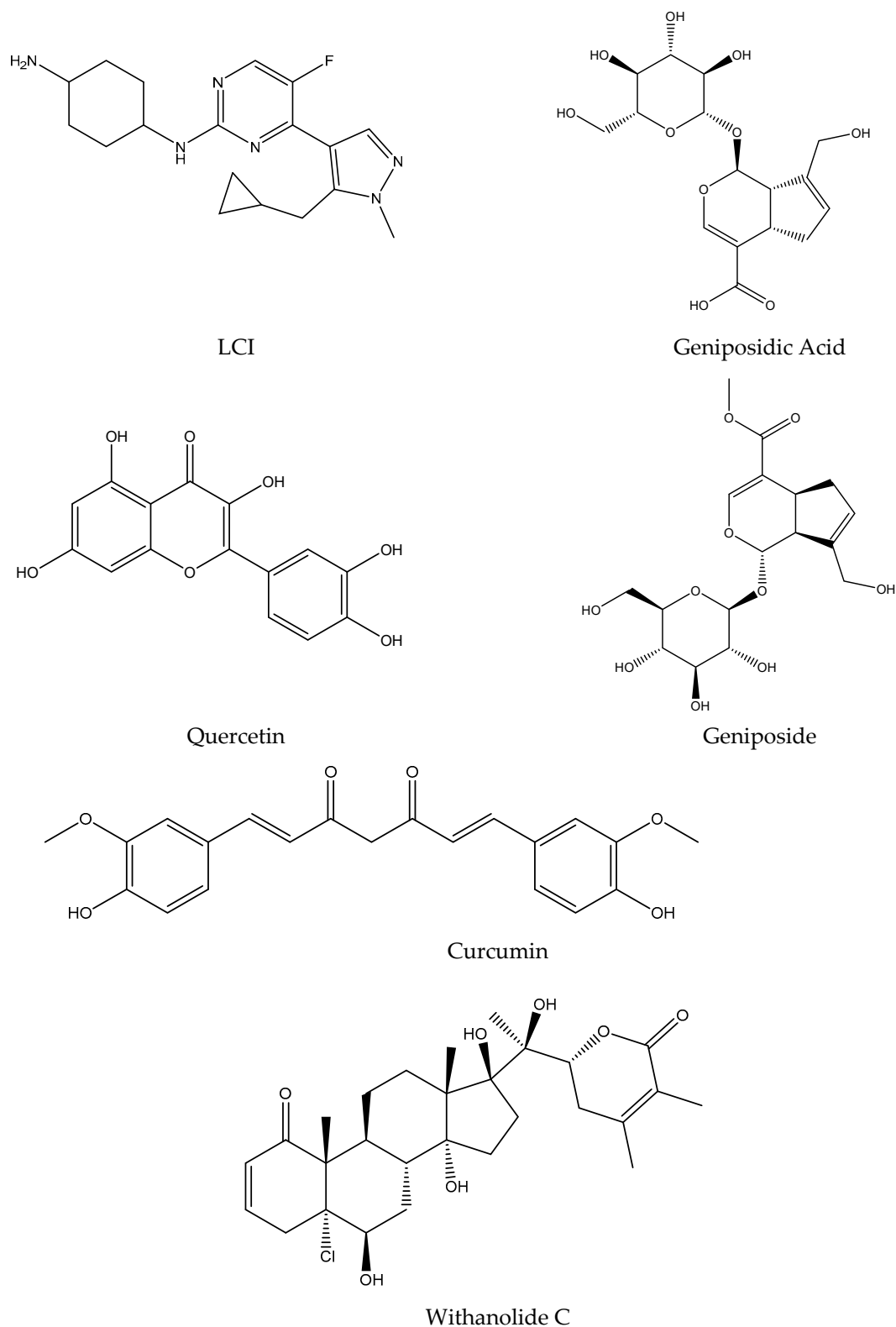


Figure 2. The chemical structures of LCI (PubChem CID: 134812748), geniposidic acid (PubChem CID: 443354), quercetin (PubChem CID: 5280343), geniposide (PubChem CID: 107848), curcumin (PubChem CID: 969516), and withanolide C (PubChem CID: 101559583). The chemical structures were drawn when considering the canonical SMILES and the isomeric SMILES obtained from the PubChem database.

3.3. Molecular Docking Results Analysis and Binding Interaction Determination

The integration of diverse molecular modeling approaches into numerous drug development programs by pharmaceutical research has facilitated the exploration of complex biological and chemical interactions. Combining computational and analytical methodologies has positively influenced identifying and developing unique and forthcoming compounds [113–115]. Molecular docking approaches are widely applied in modern drug design and study the configuration of ligands within macromolecular target attachment regions. Moreover, the strategy determines the ligand–receptor relationship’s free energy by analyzing the intermolecular interactions’ mechanism [116–119]. The XP molecular docking (grid box size: 10 Å × 10 Å × 10 Å) was conducted using the GLIDE program. The XP docked scores were measured as −11.425 kcal/mol, −13.908 kcal/mol, −10.775 kcal/mol, −9.969 kcal/mol, −9.898 kcal/mol, and −8.114 kcal/mol for the 6GZH-LCI complex (co-crystallized ligand), 6GZH-geniposidic acid complex, 6GZH-quercetin complex, 6GZH-geniposide complex, 6GZH-curcumin complex, and 6GZH-withanolide C complex, respectively (Table 1). The XP docked complexes interacted with different binding interactions, including the H-bonds and non-bonding interactions. The H-bonds interaction of 6GZH-LCI complex (CYS106, ASP109), 6GZH-geniposidic acid complex (ILE25, ALA153, ASN154, ASP104, CYS106), 6GZH-quercetin complex (CYS106, GLU107), 6GZH-geniposide complex (ASN154, CYS106, ASP109), 6GZH-curcumin complex (LYS48, CYS106, ASN154), and 6GZH-Withanolide C complex (ILE25, GLN27, ALA153, LYS48, ASP109) were demonstrated by the XP docking (Figure 3). The Pi-Pi stacking interaction was calculated (PHE103) in the 6GZH-LCI complex. Moreover, the non-bonding interaction, including polar, hydrophobic, negative charged, and positively charged interactions in the docked complexes, was demonstrated (Table 1, Figure 3).

Table 1. The XP docking scores with different binding interactions.

Protein–Ligand Complex	Docking Score (kcal/mol)	H-Bonds	Non-Bonding Interactions
6GZH-LCI complex (Co-crystallized ligand)	−11.425	CYS106, ASP109	<i>Polar:</i> GLN27, HIS108 <i>Hydrophobic:</i> ILE25, PHE30, ALA166, VAL79, ALA46, PHE103, PHE105, CYS106, LEU156 <i>Charged (Negative):</i> ASP167, ASP104, GLU107, ASP109 <i>Charged (Positive):</i> LYS48 <i>Glycine:</i> GLY26
6GZH-Geniposidic Acid complex	−13.908	ILE25, ALA153, ASN154, ASP104, CYS106	<i>Hydrophobic:</i> ALA153, LEU156, PHE30, VAL33, PHE168, ALA166, ALA46, VAL79, PHE103, PHE105 <i>Charged (Negative):</i> ASP167, ASP109 <i>Charged (Positive):</i> LYS151, LYS48 <i>Glycine:</i> GLY26 <i>Polar:</i> HIS108
6GZH-Quercetin complex	−10.775	CYS106, GLU107	<i>Hydrophobic:</i> LEU156, PHE30, VAL33, VAL79, ALA46, PHE103, PHE105, ILE25 <i>Charged (Negative):</i> ASP167, GLU107, ASP109 <i>Charged (Positive):</i> LYS48 <i>Polar:</i> HIS108
6GZH-Geniposide complex	−9.969	ASN154, CYS106, ASP109	<i>Hydrophobic:</i> LEU156, ALA25, ALA166, PHE30, VAL33, ALA46, VAL79, PHE103, PHE105 <i>Charged (Negative):</i> ASP167, ASP104, GLU107 <i>Charged (Positive):</i> LYS48
6GZH-Curcumin complex	−9.898	LYS48, CYS106, ASN154	<i>Hydrophobic:</i> ALA166, PHE168, VAL33, PHE30, ALA46, PHE103, PHE105, CYS106, LEU156, ILE25, VAL79, LEU70 <i>Charged (Negative):</i> ASP109, ASP167, GLU66 <i>Charged (Positive):</i> LYS151 <i>Glycine:</i> GLY26 <i>Polar:</i> ASN154
6GZH-Withanolide C complex	−8.114	ILE25, GLN27, ALA153, LYS48, ASP109	<i>Hydrophobic:</i> PHE30, VAL33, LEU156, ALA46, ALA166, PHE103, CYS106, VAL79 <i>Charged (Negative):</i> ASP167 <i>Glycine:</i> GLY26

3.4. ADMET Prediction and Anticipation of the Selected Ligands

In the discipline of effective therapy, a potent molecule needs to arrive at its destination in the body in a functioning state and reside there long enough for the anticipated physiological actions to occur. ADMET analysis is gradually integrated into the drug development process during the discovery phase when the number of potential substances is high but physical samples are scarce. Computer models are feasible alternatives to experimenting in this case. In this situation, computational models are valid substitutes for experimentation [10,99,120]. The new SwissADME web application provides free access to a pool of rapid yet reliable predictive model types. These include pharmacokinetics, physicochemical characteristics, drug-likeness, and medicinal chemistry affinity, including competent in-house strategies such as the iLOGP [121], BOILED-Egg [122], and Bioavailability Radar [100]. In addition, the pkCSM utilizes graph-based recognition to predict pharmacokinetic features. These represent the molecular structure and are used to construct prediction systems [101,123]. LCI, geniposidic acid, quercetin, geniposide, curcumin, and withanolide C have molecular weights of 344.43 g/mol, 374.34 g/mol, 302.24 g/mol, 388.37 g/mol, 368.38 g/mol, and 523.06 g/mol with the number of acceptor H-bonds as of 5, 10, 7, 10, 6, and 7, respectively (Table 2). Comprehension results for physicochemical properties were illustrated including the parameters POLAR (polarity), LIPO (lipophilicity), INSOLU (insolubility), SIZE (molecular size), INSATU (unsaturation), and FLEX (flexibility) (Figure 4).

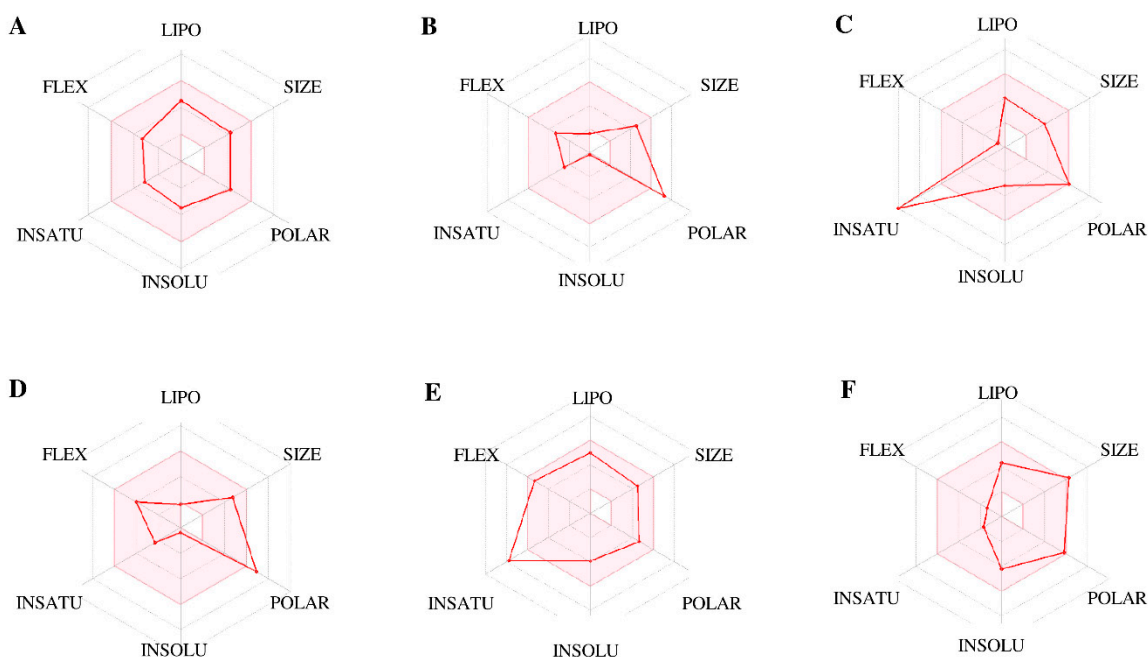


Figure 4. The physicochemical space for oral bioavailability. The bioavailability monitor supplies an initial evaluation of a molecule's drug-likeness. The colorful region represents the appropriate physicochemical environment for oral bioavailability of LCI (A), geniposidic acid (B), quercetin (C), geniposide (D), curcumin (E), and withanolide C (F). Parameters: POLAR (polarity, $20 \text{ \AA}^2 < \text{TPSA} < 130 \text{ \AA}^2$), LIPO (lipophilicity, $-0.7 < \text{XLOGP3} < +5$), INSOLU (insolubility, $0 < \text{Log S (ESOL)} < 6$), SIZE (molecular size, $150 \text{ g/mol} < \text{MW} < 500 \text{ g/mol}$), INSATU (unsaturation, $0.25 < \text{Fraction Csp3} < 1$), and FLEX (flexibility, $0 < \text{Num. rotatable bonds} < 9$).

Table 2. ADMET properties (obtained from the SwissADME and the pkCSM databases) of LCI, geniposidic acid, quercetin, geniposide, curcumin, and withanolide C.

	LCI	Geniposidic Acid	Quercetin	Geniposide	Curcumin	Withanolide C
Formula	C ₁₈ H ₂₅ FN ₆	C ₁₆ H ₂₂ O ₁₀	C ₁₅ H ₁₀ O ₇	C ₁₇ H ₂₄ O ₁₀	C ₂₁ H ₂₀ O ₆	C ₂₈ H ₃₉ C ₁ O ₇
Molecular weight (g/mol)	344.43	374.34	302.24	388.37	368.38	523.06
H-Bond acceptors	5	10	7	10	6	7
H-Bond donors	2	6	5	5	2	4
Num. rotatable bonds	5	5	1	6	8	2
TPSA (Å ²)	81.65	166.14	131.36	155.14	93.06	124.29
Fraction Csp3	0.61	0.69	0.00	0.71	0.14	0.79
Molar refractivity	95.68	82.57	78.03	86.89	102.80	135.75
LogP _{o/w} (XLOGP3)	2.40	−2.67	1.54	−2.34	3.20	2.03
LogS (ESOL)	−3.48	−0.15	−3.16	−0.38	−3.94	−4.23
Max. tolerated dose (human) (log mg/kg/day)	−0.142	1.339	0.499	0.528	0.081	−0.694
Oral rat acute toxicity (LD50 mol/kg)	2.37	2.085	2.471	2.188	1.833	2.417
Hepatotoxicity	Yes	No	No	No	No	No
Minnow toxicity (log mM)	1.21	6.62	3.721	6.612	−0.081	2.52
Blood–brain barrier (log BB)	−0.162	−1.041	−1.098	−1.281	−0.562	−1.004
Caco-2 permeability	1.344	−0.505	−0.229	0.35	−0.093	0.682
Total clearance (log ml/min/kg)	0.954	1.325	0.407	1.404	−0.002	0.023

The fraction Csp3 values of LCI, geniposidic acid, geniposide, curcumin, and withanolide C were measured as 0.61, 0.69, 0.71, 0.14, and 0.79, whereas quercetin remained nil. LCI, geniposidic acid, quercetin, geniposide, curcumin, and withanolide C contained the number of rotatable bonds as 5, 5, 1, 6, 8, and 2, respectively. Moreover, LCI, geniposidic acid, geniposide, curcumin, and withanolide C contained the H-bond donors as 2, 6, 5, 5, 2, and 4. It has long been accepted that lipophilicity is measured by the log P_{o/w} partition coefficient between n-octanol and water [124]. Several computer algorithms for determining log P_{o/w} on diverse chemical mixtures have been developed with variable degrees of efficacy. Typically, many indicators are employed to select the most reliable approaches for a particular chemical conjunction or to provide a consensus estimate [125–127]. The lipophilicity (XLOGP3) [128,129] of LCI, geniposidic acid, quercetin, geniposide, curcumin, and withanolide C were measured as 2.40, −2.67, 1.54, −2.34, 3.20, and 2.03. A soluble molecule streamlines several medication development steps, including processing and manufacturing [130]. In addition, solubility is a crucial element influencing absorption for oral-delivery-focused research endeavors. A drug designed for parenteral administration must also be highly soluble in water to give an appropriate number of active ingredients in a small volume of pharmacological dosage [131,132]. The ESOL (LogS) values [133] of LCI, geniposidic acid, quercetin, geniposide, curcumin, and withanolide C were calculated as −3.48, −0.15, −3.16, −0.38, −3.94, and −4.23. Pharmacokinetics examines the entry, circulation, and elimination of drugs from the body. How an individual responds to a particular medication is governed by the substance's underlying pharmacological properties at the site of action [134–136]. The BOILED-Egg model's conclusion allows for estimations to be established regarding passive human gastrointestinal (GI) absorption as well as blood–brain barrier (BBB) permeability [137]. A drug's penetration and carrier associations may be evaluated in vitro using human colon adenocarcinoma Caco-2 and Madin–Darby canine kidney epithelial cell types [138–141]. Confluent monolayers of cells over semi-porous filters mimic the intestinal epithelial border for penetration, carrier, and drug tests. These tests can be used in pharmaceutical investigation to predict and evaluate absorption, determine permeability mechanisms, and assess the impact of composition on drug permeability [142–145]. Caco-2 permeability values of LCI, geniposidic acid, quercetin, geniposide, curcumin, and withanolide C were estimated as 1.344, −0.505, −0.229, 0.35, −0.093, and 0.682. Systemic clearance is governed by all the metabolizing/eliminating functions of each organ, although liver and kidney clearances are the most important. By scalarizing the drug excretion frequency (amount per period) by the plasma content, plasma clearance indicates the overall capacity of the body to remove the drug [146–148].

The blood–brain barrier values (logBB) for LCI, geniposidic acid, quercetin, geniposide, curcumin, and withanolide C estimated as -0.162 , -1.041 , -1.098 , -1.281 , -0.562 , and -1.004 . For inter-species comparisons, the total body extraction ratio (0 to 1) simplifies the understanding of plasma clearance and provides a basis for comparisons across species. A drug's total clearance (for a given bioavailability) is governed solely by plasma elimination, making it the most critical pharmacokinetics for calculating the dosage necessary to preserve an equilibrium steady-state plasma level [146,149–151]. The total clearance of LCI, geniposidic acid, quercetin, geniposide, curcumin, and withanolide C were estimated as of 0.954, 1.325, 0.407, 1.404, -0.002 , and 0.023. Additionally, all selected ligands have no hepatotoxicity effects except the co-crystallized ligand, LCI.

The pharmaceutical therapy of illness has long been known to begin slowly and gradually increase the dosage. Even when treating acute and more severe diseases, doctors frequently exceed the maximum tolerated dosage (MTD) despite the lack of evidence that doing so is more likely to enhance patient outcomes [152,153]. Cardiovascular guidelines advise MTD even in prevention without clear evidence of improved outcomes for several indications, such as hypercholesterolemia [153–155]. The MTD values for LCI, geniposidic acid, quercetin, geniposide, curcumin, and withanolide C estimated as 0.142, 1.339, 0.499, 0.528, 0.081, and -0.694 . To determine the acute toxicity of different substances, lethal dosage estimates (LD50) are generally employed. The LD50 is the portion of a chemical that eradicates 50% of a group of test animals if given at once [156]. The oral rat acute toxicity (LD50) values for LCI, geniposidic acid, quercetin, geniposide, curcumin, and withanolide C were estimated as 2.37, 2.085, 2.471, 2.188, 1.833, and 2.417.

3.5. Molecular Dynamics

Carrying out molecular dynamics simulations, we first implemented the steps by running the scripts for evaluating the stabilities of backbone atoms of the targeted protein as presented in Figure 5A. The apo and holo forms of the CDK9/cyclinT1 were introduced to 100 ns MD simulations in an explicit solvated system. Figure 5A shows RMSD values for the main protease backbone for the apo and holo status of the CDK9/cyclinT1. The protein backbone residues showed low fluctuations before equilibration for all systems (apo and holo). For the RMSD of the backbone atoms of apo, LCI-bound, geniposidic-acid-bound, geniposide-bound and withanolide-bound CDK9/cyclinT1 were stable throughout the MD simulation study. However, the RMSD of backbone atoms for the mentioned systems showed minimal fluctuation between 0.2 and 0.44 nm during the MD simulation (Figure 5A). In comparison, the quercetin-bound and curcumin-bound CDK9/cyclinT1's backbone atoms exhibited significant fluctuations after 53 ns in the MD simulation study (Figure 5A). This could be because of how curcumin is positioned in the active site, which has two rings connected by seven rotatable links, one deep inside the binding site and the other near the active site's gate. Even though quercetin's stiffness led to considerable oscillations, it does include one rotatable bond. As a result, quercetin may result in a more relaxed deformation of the CDK9/cyclinT1 active site.

The RMSD of bound ligands was also analyzed to shed light on the actual mechanism of action of studied ligands. The RMSD plot suggests that the binding of quercetin and curcumin destabilized the CDK9/cyclinT1 and led to more structural deviations from its native conformation (Figure 5A). RMSD of the curcumin revealed that curcumin has the highest degree of fluctuation inside the binding site of CDK9/cyclinT1. This can be due to the orientation of curcumin in the active site, which contains two rings linked with seven rotatable bonds, one located deep inside the binding site and another located on the gate of the active site. While the rigidity of quercetin caused significant fluctuations, quercetin contains one rotatable bond. Thus, quercetin can cause deformation of the active site of CDK9/cyclinT1 to be more relaxed. On the other hand, it is worth noting that withanolide had very stable dynamic behavior inside the binding site of CDK9/cyclinT1 (Figure 5B).

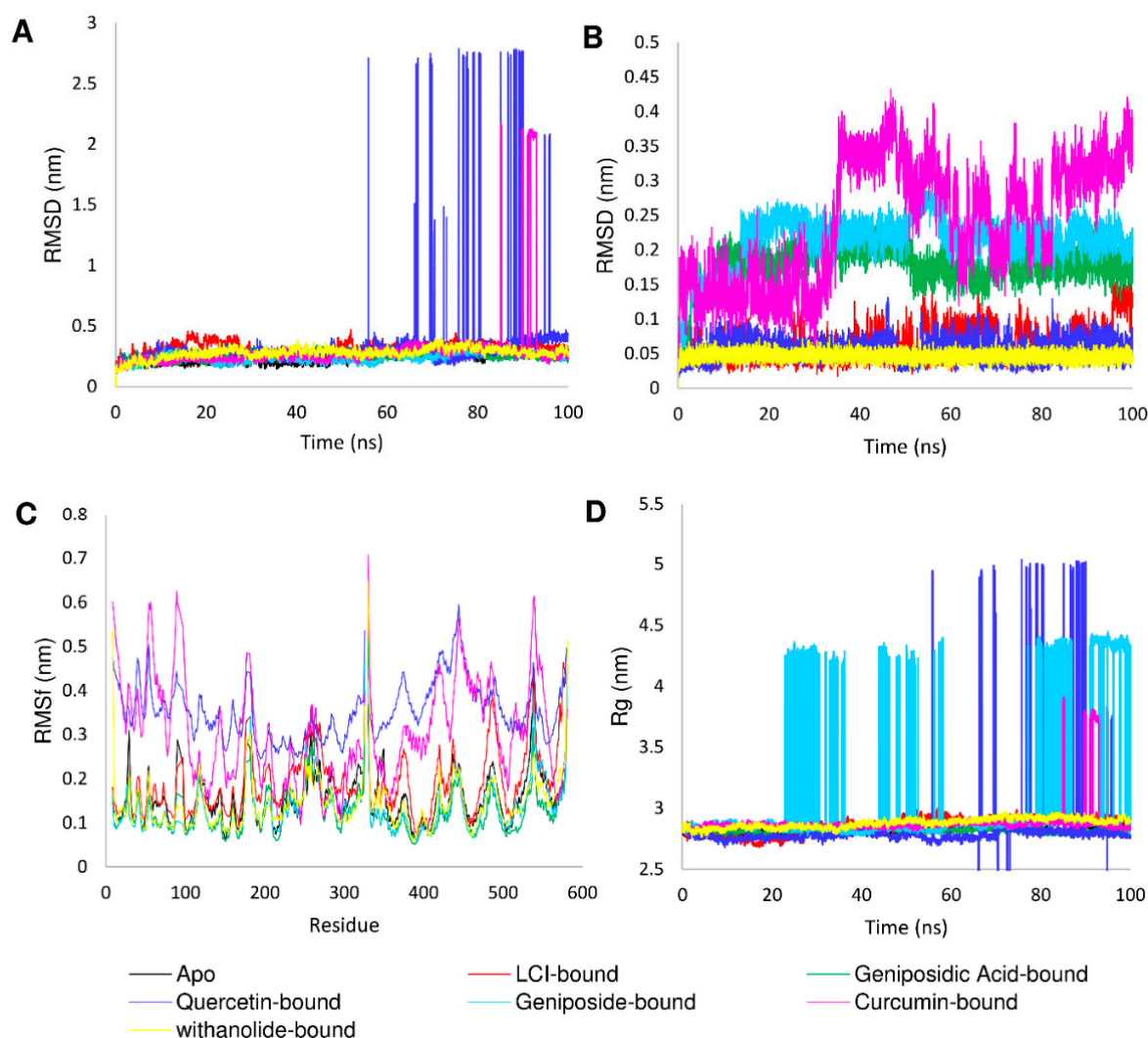


Figure 5. (A) RMSD of backbone atoms for apo and holo forms of protein, (B) RMSD of ligands atoms, (C) RMSF of backbone atoms of apo and holo forms of protein, (D) Rg of the protein in apo and holo forms. The CDK9/cyclinT1 apo and holo versions were added to 100 ns MD simulations in an explicit solvated system. Before equilibration for all systems, the protein backbone residues exhibited little variations (apo and holo). LCI-bound, geniposidic-acid-bound, geniposide-bound, and withanolide-bound CDK9/cyclinT1 remained constant during the MD simulation research for the RMSD of the backbone atoms of apo. Curcumin exhibits the most considerable level of variation inside the CDK9/cyclinT1 binding site, according to RMSD measurements. However, it is essential to remember that withanolide had remarkably steady dynamic behavior inside the binding site of CDK9/cyclinT1. The Rg plot showed that the CDK9/cyclinT1 bound to withanolide, geniposidic acid, and LCI attained tighter packing.

Vibrations and fluctuation are not random but depend mainly on the flexibility of the local and global structure. Therefore, the root-mean-square fluctuation (RMSF) of the CDK9/cyclinT1 in apo and holo forms was analyzed to ascertain the average fluctuation of all residues during the simulation (Figure 5C). The RMSF plot showed that higher residual fluctuations were present in most regions of CDK9/cyclinT1 due to binding to quercetin and curcumin. In contrast, the residual fluctuations were minimized upon binding geniposidic acid, geniposide, and withanolide in most regions (Figure 5C).

The radius of gyration (Rg) is the main parameter to analyze the volume of a protein's tertiary structure. It has been utilized to shed light on the global stability of a protein in a biological system. The higher value of the radius of gyration of studied

proteins means less tight packing. The average R_g values for free quercetin, curcumin, and geniposide were higher among the studied ligands. The R_g plot indicated that the withanolide-bound, geniposidic-acid-bound, and LCI-bound CDK9/cyclinT1 reached more tight packing (Figure 5D).

We can analyze the selectivity and potentiality by assessing hydrogen bonding between a protein and ligands as a critical aspect of molecular recognition. Additionally, it is used to validate the stability of the docked ligands. It was found that LCI had the highest average of hydrogen bonds (3.51). The second was for geniposide, with a 2.57 hydrogen bond, while the lowest average was for curcumin, with a 1.5 hydrogen bond (Figure 6).

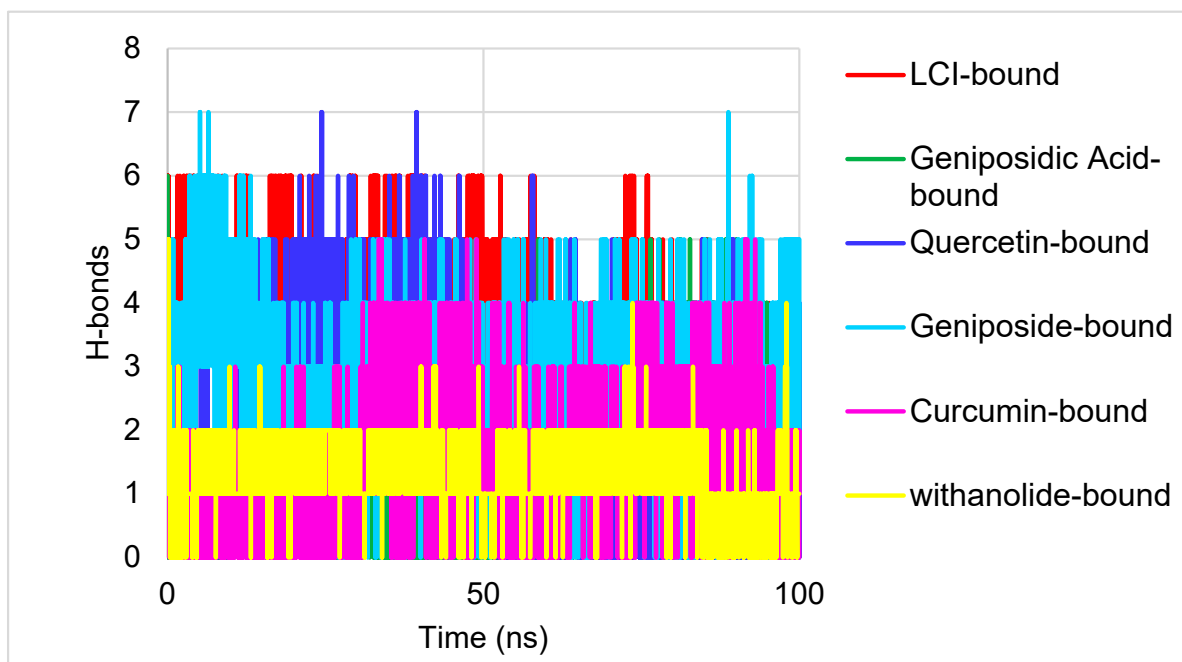


Figure 6. Number of H-bonds during 100 ns MD simulations. LCI was shown to have the most sumptuous moderate hydrogen bond count (3.51), followed by geniposide (2.57 hydrogen bonds) and curcumin (1.5 hydrogen bonds).

3.6. PCA and FEL Analysis

Principal component analysis (PCA) was carried out to describe the predominant movement of the protein structures for each of the seven simulations. The first two principal components for each model structure explained more than 80% of the system's motion. We plotted the populated cluster motions for each system to visualize the 2D projection of the first two principal components (Figure 7A,C,E,G,I,K,M). The apo, LCI-bound, geniposidic-acid-bound, and withanolide-bound CDK9/cyclinT1 exhibited fewer collective movements (Figure 7A,C,E,M). In contrast, quercetin-bound, geniposide-bound, and curcumin-bound CDK9/cyclinT1 showed a disorganized collective movement (Figure 7G,I,K).

The free energy landscape or Gibbs free energy landscape shows the global energy minima conformations defined as each system's lowest stable energy state. The results of the free energy landscape are shown in Figure 7B,D,F,H,J,L,N. The dark blue spots indicate the energy minima and energetically favored protein conformations. The shallow energy basin was also noticed during the simulation, indicating low stability of the protein–ligand complex. Two distinct broad valleys were observed in the apo and LCI-bound CDK9/cyclinT1. At the same time, withanolide-bound CDK9/cyclinT1 had a single and broad valley of energy. Interestingly, geniposidic-acid-bound had a single and precise deep spot of the blue region observed.

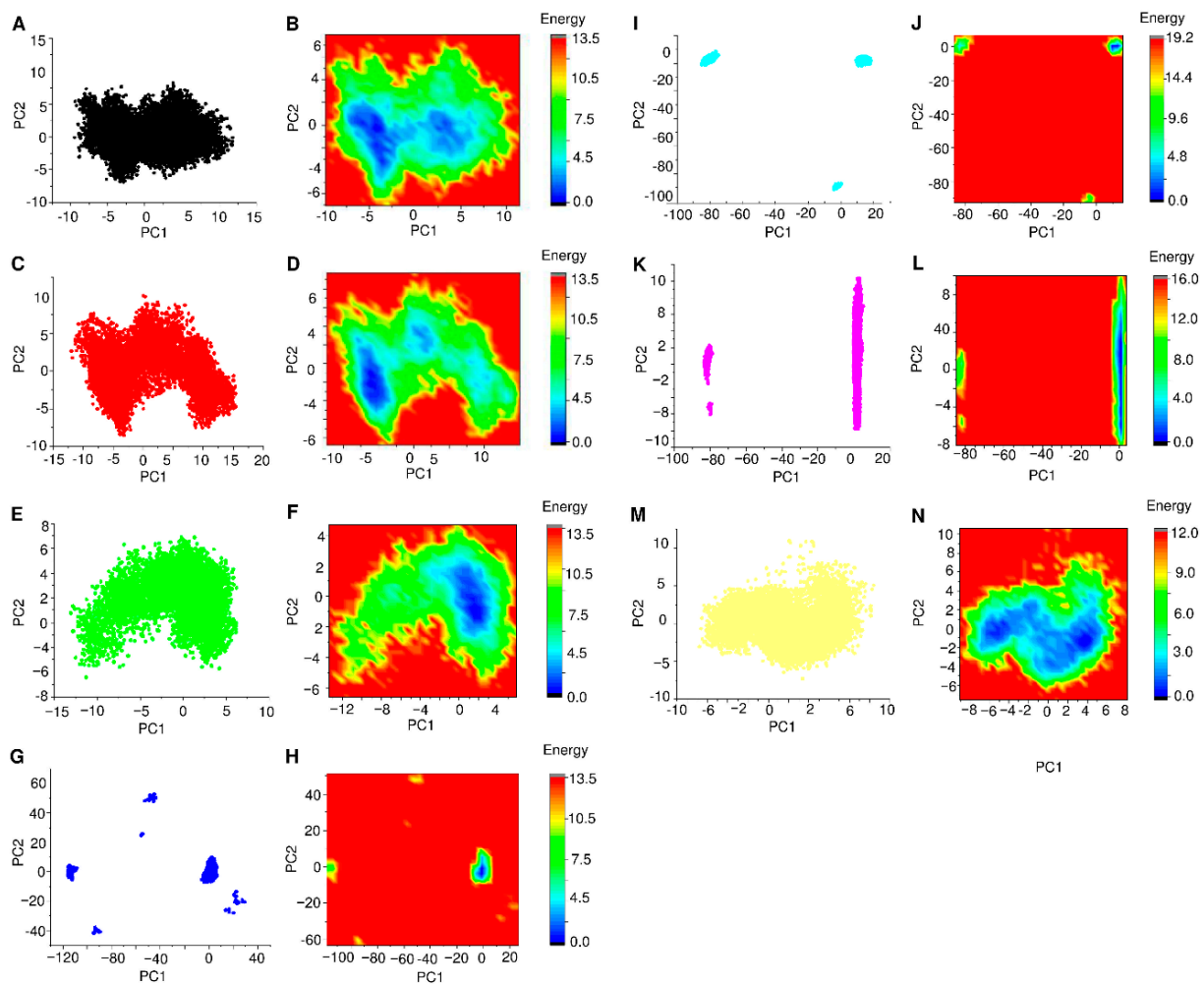


Figure 7. PCA of (A) apo, (C) LCI-bound, (E) geniposidic-acid-bound, (G) quercetin-bound, (I) geniposide-bound, (K) curcumin-bound and (M) withanolide-bound CDK9/cyclin T1. Free energy landscapes of (B) apo, (D) LCI-bound, (F) geniposidic-acid-bound, (H) quercetin-bound, (J) geniposide-bound, (L) curcumin-bound, and (N) withanolide-bound CDK9/cyclin T1. Two large troughs were found in the apo and LCI-bound CDK9/cyclinT1. Simultaneously, withanolide-bound CDK9/cyclinT1 exhibited a single and large energy valley. Interestingly, geniposidic-acid-bound has a single, exact deep-blue patch seen.

3.7. Network Pharmacology Analysis

3.7.1. PPI Network Analysis

Six hundred and nine target genes interacting with LCI, geniposidic acid, quercetin-bound, geniposide, curcumin, and withanolide were collected from the Swiss Target Prediction and DIGEP-Pred. Six hundred and nine target genes were exported to the string database and were used to explore the interaction relationship between core targets. Then, a PPI network was created using Cytoscape (Figure 8). The 609 candidate genes were connected to establish an initial PPI network using Cytoscape 3.8.3 that included 563 nodes and 6471 edges, and 46 isolated target genes were removed (Figure 8). In addition, the top one protein–protein interacting cluster was constructed (Figure 5A), conducted by MCODE of Cytoscape to identify the highly interacting nodes. It contained 42 nodes and 617 edges, as presented in Figure 8A (red nodes). To validate the results, we further used Cytoscape-hubba for identifying hub targets. We obtained a network of 42 nodes and 699 edges, as illustrated in Figure 8B (colored nodes). Then, the target genes from MCODE and Cyto-hubba were merged to obtain a single network with 51 target genes and 855 edges (Figure 9). As can be seen from Figure 9, CASP3 (degrees = 50), KRAS

(degrees = 50), MTOR (degrees = 50), JUN (degrees = 49), HIF1A (degrees = 48), CCND1 (degrees = 48), HSP90AA1 (degrees = 48) and BCL2L1 (degrees = 47). Additionally, CASP3, KRAS, MTOR, JUN, HIF1A, CCND1, HSP90AA1, and BCL2L1 had the highest betweenness centrality value. The 51 target genes were exported into the DAVID database for KEGG pathway enrichment.

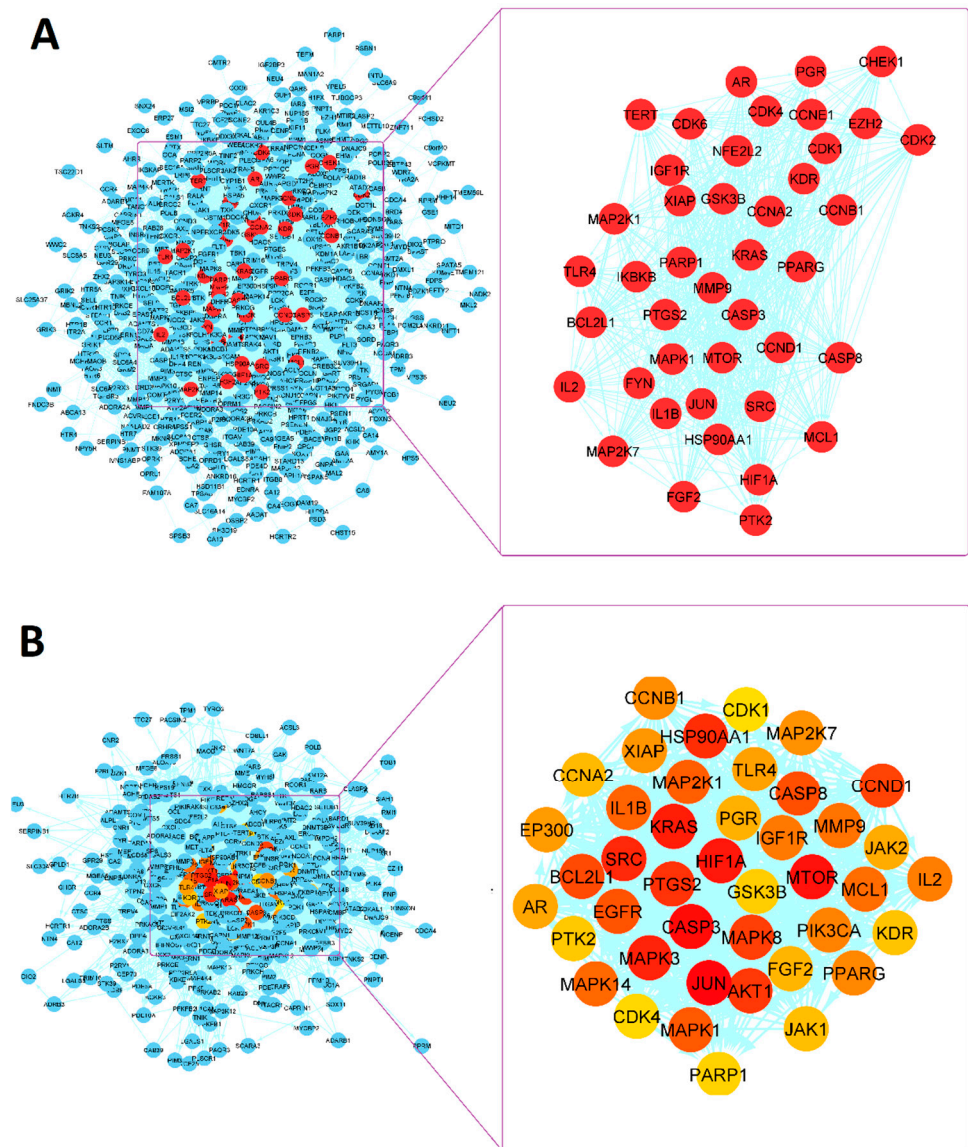


Figure 8. Protein–protein interaction network of common genes of obtained target genes of nominated compounds. A total of 609 target genes were exported to the string database to investigate the interactions between core targets. The PPI network was then developed using Cytoscape as a visualization tool. (A) The top protein–protein interacting cluster was constructed to identify the highly interacting nodes that contained 42 nodes (red nodes) and 617 edges. (B) Cytoscape-hubba tool was employed to validate the results, generating a network of 42 nodes (colored nodes) and 699 edges.

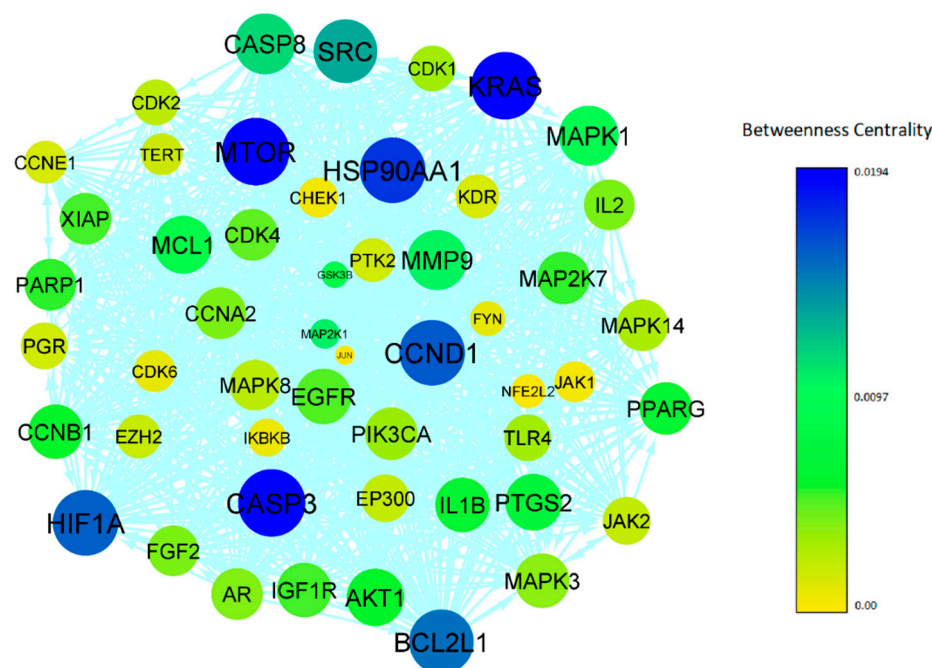


Figure 9. The network of the core target genes. A single network with 51 target genes and 855 edges was created by combining the target genes retrieved from MCODE and Cyto-hubba. The 51 target genes were imported into the DAVID database to enhance KEGG pathways that generated the network of the core target genes.

3.7.2. KEGG Pathway Enrichment Analysis

We conducted a KEGG pathway enrichment analysis. The significant pathways include cancers ($-\log p = 26.3045$, target connections count = 33), Hepatitis B ($-\log p = 23.1688$, connections count = 23), PI3K-Akt signaling pathway ($-\log p = 19.76$, target connections count = 27), prostate cancer ($-\log p\text{-value} = 19.55$, and target connections count = 18), pancreatic cancer ($-\log p\text{-value} = 16.7399$, target connections count = 15), proteoglycans with $-\log p$ value (15.89) and target connections (count = 20), TNF signaling pathway ($-\log p\text{-value} = 14.99$, and target connections count = 16), etc. These pathways are crucial in initiating tumor cell growth and differentiation and promoting tumor cell progression. Then, the top 20 signaling pathways were visualized in Figure 10. The LCI, geniposidic acid, quercetin, geniposide, curcumin, and withanolide, core targets, and 20 pathways were imported into Cytoscape to create a “compound-target-pathway” network diagram and visualize it (Figure 11). The compound-target-pathway had 128 nodes and 1302 edges. The network analysis showed that curcumin had more significant interaction for targets genes with degree 20, followed by withanolide (degree = 19), LCI (degree = 16), geniposidic acid (degree = 12), quercetin (degree = 3) and geniposide (degree = 1).

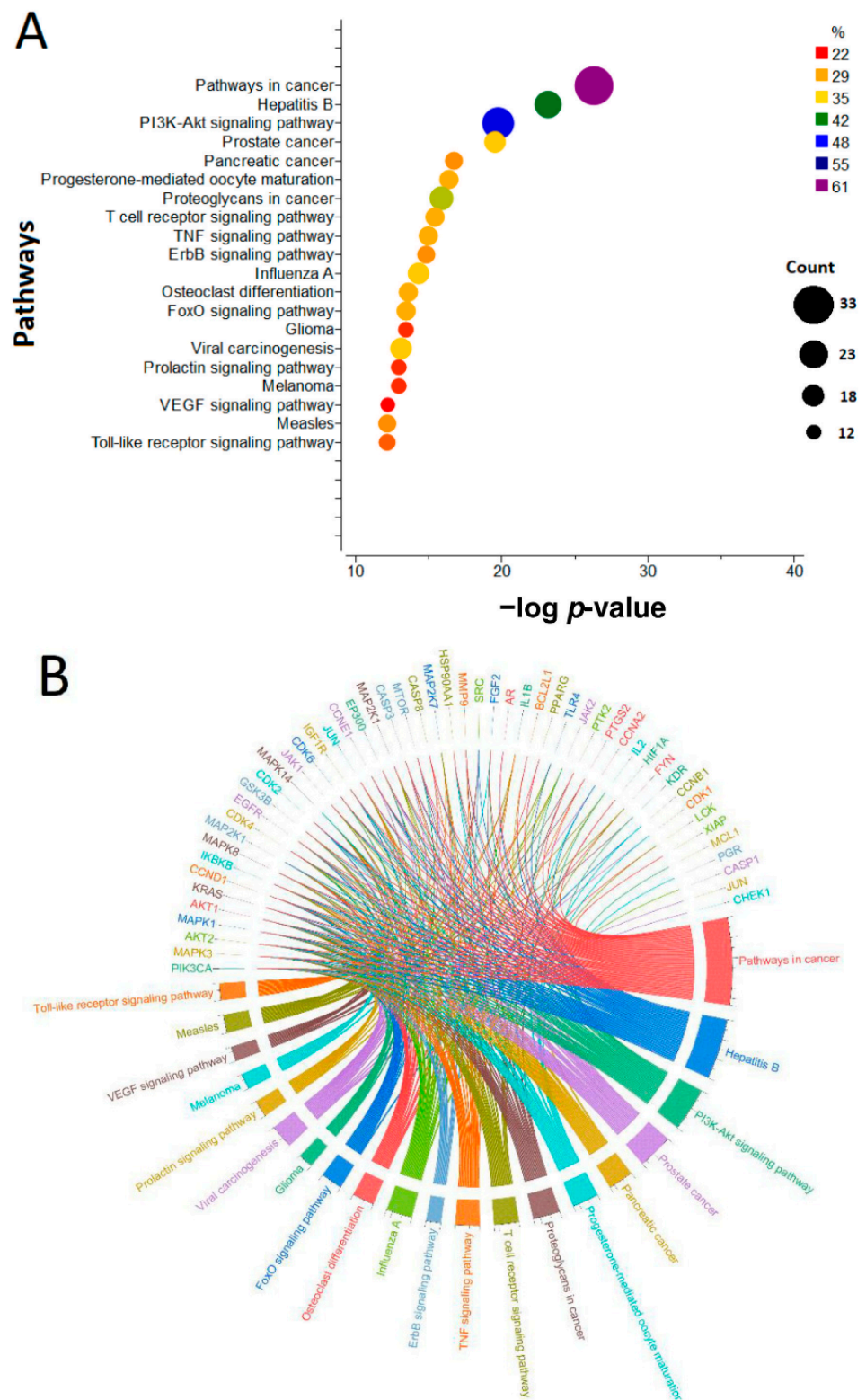


Figure 10. (A) Enrichment analysis on KEGG pathways of key targets from active compounds. (B) Core targets linked to top 20 KEGG pathways in Chord plot. Note: The size of the dots indicates the number of genes and the color of the dots represents the percentage.

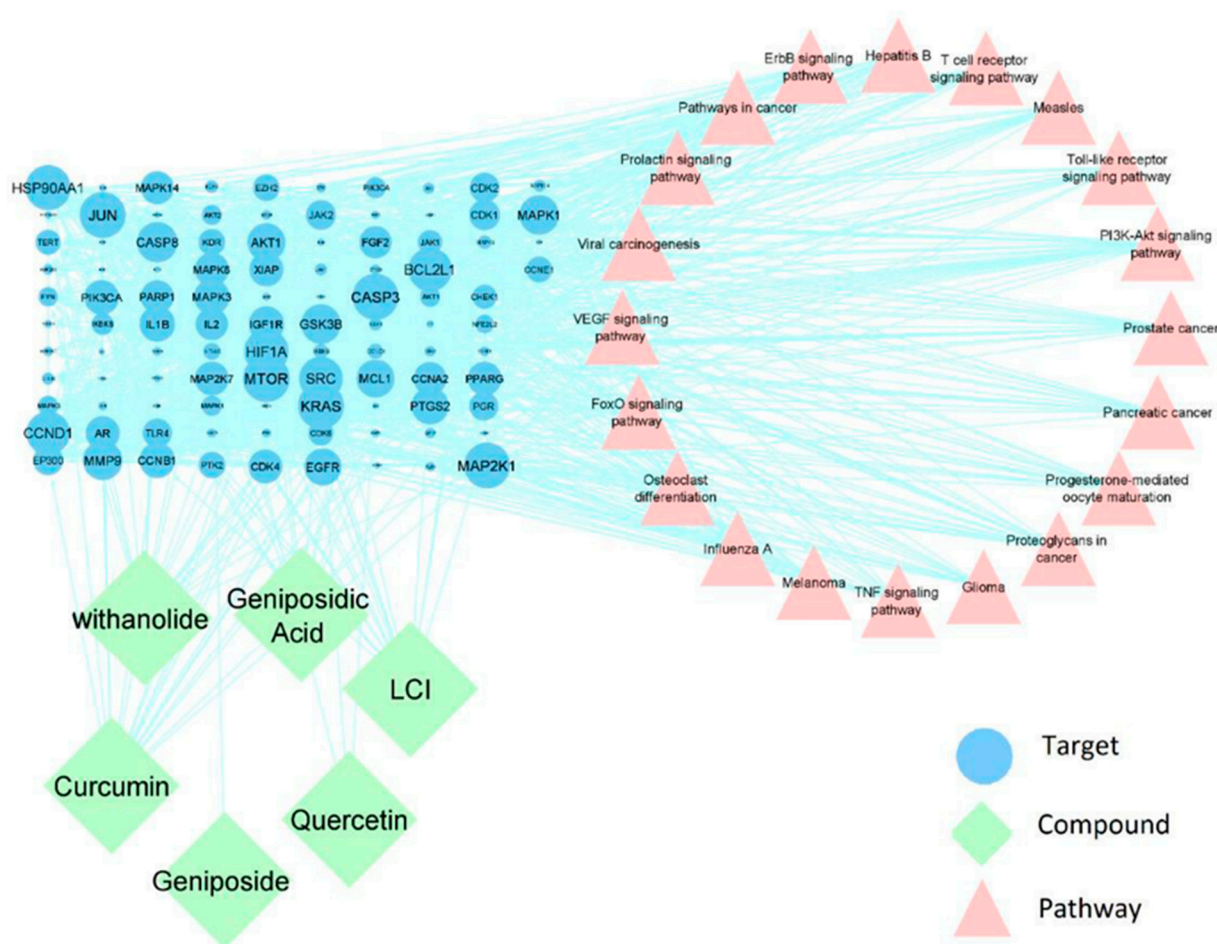


Figure 11. The pathways for the selected compounds with the target genes. The illustration describes the promising target gene-triggered pathway networks for the selected ligands. These pathways are vital in originating tumor, tumor cell growth, differentiation, and promoting tumor cell progression.

4. Discussion

In the early stages of the drug lead development process, computational approaches are a potent and well-established tool. High-throughput molecular docking is one of these methods, and it has proven to be quite effective in locating new bioactive substances within sizable chemical libraries [157,158]. Protein and the selected ligands are prepared before performing molecular docking. Each small molecule's preferred binding mode within a target binding site is evaluated throughout the docking process. A docking score indicates how likely the ligand molecule will attach. The techniques also provide insight into how a particular 'hit' may be altered to enhance protein–ligand interactions, which can be used to direct lead optimization. The strategy was very tempting since it had the potential to save time and money in comparison to experimental alternatives [119,159]. Geniposidic acid interacted with the protein 6GZH (docking score of -13.908 kcal/mol) and demonstrated high affinity compared to other ligands (Table 1; Figure 3), LCI (-11.425 kcal/mol), quercetin (-10.775 kcal/mol), geniposide (-9.969 kcal/mol), curcumin (-9.898 kcal/mol), and withanolide C (-8.114 kcal/mol).

To speed up the transformation of hits and leads into qualified development candidates, the evaluation of physicochemical and pharmacological characteristics is carried out at the early stages of drug discovery [160–162]. Over the years, qualities linked to ADMET have emerged as one of the most crucial factors to consider when evaluating the hazards or effects of these substances on the human body [99,163,164]. Withanolide C (523.06 g/mol) demonstrated a violation in molecular weight (<500 g/mol) as of “the rule of 5” compared to other ligands [165]. Other parameters of “the rule of 5” include H-bond donors (not

more than 5), and H-bond acceptors (not more than 10) are maintained accordingly [165]. TPSA, which uses functional group contributions based on a sizable database of structures, is a practical way to estimate polar surface area without determining the appropriate biological conformation or conformations or computing the ligand's three-dimensional structure [166,167]. Geniposidic acid, quercetin, geniposide, and withanolide C denote polarity violation ($20 \text{ \AA}^2 < \text{TPSA} < 130 \text{ \AA}^2$) compared to other ligands (Table 2, Figure 4). More than 140 angstroms squared polar surface areas of molecules make them challenging to penetrate cell membranes [168]. A TPSA of less than 90 \AA^2 is typically required for chemicals to cross the BBB and subsequently act on receptors in the CNS [169].

The idea of drug-likeness has been widely utilized to screen out compounds with undesired qualities and inferior ADMET profiles based on assessments of the physicochemical properties and structural features of current small organic medicines or/and drug prospects. The drug-likeness of a molecule is an essential consideration during the early stages of drug development. It is defined as the resemblance of chemicals and medications [10,170]. The standard fraction Csp3 value is needed at a minimum of 0.25 (fraction Csp3 ≥ 0.25) with the correlation of sp³-hybridized carbons for saturation [10,100]. Quercetin and curcumin violated the fraction Csp3 parameter (fraction Csp3 ≥ 0.25) compared to others.

A medicine's capacity to dissolve in aqueous media is called its solubility. The highest concentration of a material that can be entirely dissolved in a particular solvent at a specific temperature and pressure level is referred to as drug solubility [133,171,172]. The LogS (ESOL) value should not overreach 6.0 for the solubility of a ligand [133]. All the selected ligands maintained the solubility parameter. Lipophilicity plays an essential role in drug discovery and design. Lipophilicity is a critical physicochemical feature that influences ADMET properties and the overall appropriateness of drug candidates [124]. Controlling physicochemical parameters such as lipophilicity within a defined optimum range has increased compound quality and the chances of medicinal efficacy. Moreover, the XLOGP3 value is needed from -0.7 to $+6.0$ to maintain lipophilicity [173]. LCI, quercetin, curcumin, and withanolide C maintained the XLOGP3 parameter of lipophilicity compared to other ligands (Table 2).

The science of pharmacokinetics examines how drugs enter, move through, and leave the body. The pharmacological features of a drug at the site of action dictate how a person reacts to it [174,175]. The BOILED-Egg model predicts passive human gastrointestinal (GI) absorption and blood–brain barrier (BBB) penetration. All of the individuals chosen have high GI absorption rates and negative BBB permeant characteristics. Evaluation of active efflux across biological membranes, such as from the brain or the gastrointestinal wall to the lumen, depends on whether substances are substrates or non-substrates for the permeability glycoprotein (P-gp), considered to be the most crucial member of the ABC-transporters [122,176–178]. Hepatotoxicity caused by antituberculosis medications is a significant adverse response that can result in considerable morbidity and, in rare cases, death. This type of toxicity may affect the outcome of TB treatment in some individuals [179–181]. The co-crystallized ligand LCI is predicted to have hepatotoxicity compared to other selected ligands.

Molecular dynamics (MD) simulations may offer a plethora of energetic data on interactions between proteins and ligands in addition to a wealth of dynamical data on biomacromolecules [182]. Such knowledge is crucial for determining the target's structure–function connection and the fundamentals of protein–ligand interactions and directing the drug discovery and design processes. As a result, MD simulations have been successfully utilized at every stage of contemporary drug research [183,184]. RSMD is a widely employed metric for comparing values (sample or population values) predicted by a model or estimated values observed. The RMSD is the quadratic mean of the square root of the second sample moment of the discrepancies between expected and observed values. When computations are made outside the data sample used for the estimate, the deviations are referred to as errors (or prediction errors) instead of residuals [185,186]. The RMSD combines the sizes of forecasts' mistakes for different data points into a single indicator

of predictive power. Since RMSD is scale-dependent, it should only be used to evaluate predicting errors of several models for a single dataset and not between datasets [187,188]. The average distance between the atoms of overlaid proteins (often the backbone atoms) is measured by the RMSD. Be aware that RMSD calculations can be used to analyze smaller chemical molecules and other non-protein compounds [185,189]. CDK9/cyclinT1 'apo' and 'holo' arrangements were subjected to 100 ns MD simulations in an unambiguous solvated system with RMSD (Figure 5). The RMSD of the backbone atoms of apo, LCI-CDK9/cyclinT1, geniposide-CDK9/cyclinT1, and withanolide-CDK9/cyclinT1 complex remained steady during the MD simulation research. The RMSD of backbone atoms for the described systems, on the other hand, fluctuated between 0.2 and 0.44 nm during the MD simulation (Figure 5). Curcumin exhibited the most considerable variation inside the CDK9/cyclinT1 binding site, according to RMSD measurements. This could be because of how curcumin is arranged in the active site, which has two rings connected by seven rotatable links, one deep inside the binding site and the other near the active site's gate. However, it is essential to remember that withanolide had remarkably steady dynamic behavior inside the binding site of CDK9/cyclinT1. Due to binding to quercetin and curcumin, the RMSF plot demonstrated that more significant residual fluctuations are present in most CDK9/cyclinT1 areas. On the other hand, in the majority of locations, binding geniposidic acid, geniposide, and withanolide reduced the residual fluctuations. The Rg plot also showed that the CDK9/cyclinT1 coupled with withanolide, geniposidic acid, and LCI attained more secure packing (Figure 5). LCI was shown to have the most outlandish average hydrogen bond count (count as of 3.51), followed by geniposide (count as of 2.57 hydrogen bonds) and curcumin (count as of 1.5 hydrogen bonds) (Figure 6).

A potent theoretical paradigm for examining, comprehending, and forecasting the conformational characteristics of biomolecules is provided by statistical thermodynamics. The primary quantity, which comprises the intramolecular and solvation-free energy, is the prospect of mean strength, also known as adequate energy as a configuration function. Molecular-mechanics-style functions are a reasonable way to characterize the intramolecular potential [190,191]. Although describing the unrestricted solvation power is more challenging, useful findings may be achieved using straightforward approximations. These calculations have been used to determine how much intramolecular energy contributes to protein stability and to understand how thermodynamic properties of protein folding, such as heat capacity, first came about. The thermodynamics, as well as the kinematics of any molecular activities in solution, are driven by the FEL. The coordinates of each atom in a target molecule serve as the point on a graph representing the free energy over the arrangement region [192–194]. Two unique large troughs in CDK9/cyclinT1 were seen in the apo and LCI-bound forms. At the same time, CDK9/cyclinT1 coupled with withanolide possesses a single, wide valley of energy. Surprisingly, a single, deep point of the blue region may be seen in geniposidic-acid-bound CDK9/cyclinT1 (Figure 7).

An emerging field called network pharmacology (NP), which utilizes computational biological tools to merge system biology and genomic technology, is helpful in drug development. Network pharmacology is a method that can explain intricate connections between biological systems, medications, and disorders [195,196]. Protein–protein interactions (PPIs) are potential targets for drug development because they are connected to critical cellular processes and pathways. This assurance, however, has not been fulfilled in the case of small-molecule medications. Due to this, many PPI surfaces are physically incapable of supporting the binding of tiny drug-like compounds [197,198]. The chosen protein and ligand PPI interactions were carried out. From the Swiss Target Prediction and DIGEP-Pred, 689 target genes interacting with LCI, geniposidic acid, quercetin, geniposide, curcumin, and withanolide were gathered (Figure 8) with the networks of the core target genes (Figure 9). Genes, small molecules, proteins, and other molecular objects are mapped to networks of molecular interactions, reactions, and relationships using the KEGG mapping procedure [199,200]. Enrichment examination on KEGG pathways of crucial targets

from active substances was investigated for the chosen ligands (Figure 10). Moreover, the pathways for the preferred compounds with the target genes were anticipated (Figure 11).

LCI-bound, geniposidic-acid-bound, geniposide-bound, and withanolide-bound CDK9/cyclinT1 remained constant during the MD simulation research for the RMSD of the backbone atoms of apo. The Rg plot showed that the CDK9/cyclinT1 bound to withanolide, geniposidic acid, and LCI attained more secure packing. While in the majority of the locations, the binding of geniposidic acid, geniposide, and withanolide reduced the residual fluctuations. On the other hand, there were noticeable variations in the backbone atoms of CDK9/cyclinT1 that were linked to quercetin and curcumin. Geniposidic acid is a more potential CDK9 inhibitor than other ligands, documented by comparing molecular docking score and binding interactions with protein, ADMET attributes, MD simulation investigation, PCA, and FEL analysis.

5. Conclusions

CDK blockers have been developed to treat various diseases caused by abnormalities in CDKs, which are critical for cell formation, gene transcription, and other processes. In addition, CDK9 regulates short-lived anti-apoptotic genes that are essential for cancer cell survival. As a result, blocking CDK9 has emerged as a possible cancer therapy. Natural-derived compounds, including geniposidic acid, quercetin, geniposide, curcumin, and withanolide C, interacted with the protein with increased affinity. Geniposidic acid has a high binding affinity (−13.908 kcal/mol) with the protein CDK9 compared to other ligands. Moreover, the network-pharmacology-based analysis of the selected ligands demonstrated different signaling pathways for cancers. This study showed that the selected compounds are considered potential CDK9 blockers through computational approaches. In addition to encouraging medicinal chemistry experts to conduct relevant studies on these prospective natural lead compounds, the outcomes will assist future preclinical, nonclinical, and clinical investigations involving these molecules.

Author Contributions: A.S.M.S.: conceptualization, formal data analysis, and original draft writing. K.A.-K.: MD simulation study and original draft writing. A.S.M.S., K.A.-K., H.A. and J.-G.C.: formal data analysis and original draft preparation. M.H.: visualization, supervision, and proofreading and copy editing. S.-S.L.: Supervision and project fund acquisition. All authors have read and agreed to the published version of the manuscript.

Funding: This research was supported by the Brain Pool (BP) program (2021H1D3A2A01099303) and the Basic Science Research Program (2021R1I1A3054773) funded by the Ministry of Science and ICT and the Ministry of Education, respectively, through the National Research Foundation of Korea (NRF).

Conflicts of Interest: The authors declare no conflict of interest.

References

1. Schafer, K.A. The cell cycle: A review. *Vet Pathol* **1998**, *35*, 461–478. [[CrossRef](#)] [[PubMed](#)]
2. Coffman, J.A. Cell cycle development. *Dev. Cell* **2004**, *6*, 321–327. [[CrossRef](#)] [[PubMed](#)]
3. Murray, A. Cell cycle checkpoints. *Curr. Opin. Cell. Biol.* **1994**, *6*, 872–876. [[CrossRef](#)] [[PubMed](#)]
4. Kar, S. Unraveling Cell-Cycle Dynamics in Cancer. *Cell Syst.* **2016**, *2*, 8–10. [[CrossRef](#)] [[PubMed](#)]
5. Barnum, K.J.; O'Connell, M.J. Cell cycle regulation by checkpoints. *Methods Mol. Biol.* **2014**, *1170*, 29–40.
6. Lim, S.; Kaldis, P. Cdks, cyclins and CKIs: Roles beyond cell cycle regulation. *Development* **2013**, *140*, 3079–3093. [[CrossRef](#)] [[PubMed](#)]
7. Wenzel, E.S.; Singh, A.T.K. Cell-cycle Checkpoints and Aneuploidy on the Path to Cancer. *In Vivo* **2018**, *32*, 1–5.
8. Zhang, M.; Zhang, L.; Hei, R.; Li, X.; Cai, H.; Wu, X.; Zheng, Q.; Cai, C. CDK inhibitors in cancer therapy, an overview of recent development. *Am. J. Cancer Res.* **2021**, *11*, 1913–1935.
9. Sofi, S.; Mehraj, U.; Qayoom, H.; Aisha, S.; Asdaq, S.M.B.; Almilaibary, A.; Mir, M.A. Cyclin-dependent kinases in breast cancer: Expression pattern and therapeutic implications. *Med. Oncol.* **2022**, *39*, 106. [[CrossRef](#)] [[PubMed](#)]
10. Tian, S.; Wang, J.; Li, Y.; Li, D.; Xu, L.; Hou, T. The application of in silico drug-likeness predictions in pharmaceutical research. *Adv. Drug Deliv. Rev.* **2015**, *86*, 2–10. [[CrossRef](#)] [[PubMed](#)]

11. Malumbres, M.; Harlow, E.; Hunt, T.; Hunter, T.; Lahti, J.M.; Manning, G.; Morgan, D.; Tsai, L.-H.; Wolgemuth, D.J. Cyclin-dependent kinases: A family portrait. *Nat. Cell Biol.* **2009**, *11*, 1275–1276. [[CrossRef](#)]
12. Bury, M.; Calvé, B.L.; Ferbeyre, G.; Blank, V.; Lessard, F. New Insights into CDK Regulators: Novel Opportunities for Cancer Therapy. *Trends Cell Biol.* **2021**, *31*, 331–344. [[CrossRef](#)] [[PubMed](#)]
13. Morales, F.; Giordano, A. Overview of CDK9 as a target in cancer research. *Cell Cycle* **2016**, *15*, 519–527. [[CrossRef](#)]
14. Baumli, S.; Lolli, G.; Lowe, E.D.; Troiani, S.; Rusconi, L.; Bullock, A.N.; Debreczeni, J.; Knapp, S.; Johnson, L.N. The structure of P-TEFb (CDK9/cyclin T1), its complex with flavopiridol and regulation by phosphorylation. *EMBO J.* **2008**, *27*, 1907–1918. [[CrossRef](#)]
15. Yik, J.H.; Chen, R.; Nishimura, R.; Jennings, J.L.; Link, A.J.; Zhou, Q. Inhibition of P-TEFb (CDK9/Cyclin T) kinase and RNA polymerase II transcription by the coordinated actions of HEXIM1 and 7SK snRNA. *Mol. Cell* **2003**, *12*, 971–982. [[CrossRef](#)]
16. Pandey, S.; Djibo, R.; Darracq, A.; Calendo, G.; Zhang, H.; Henry, R.A.; Andrews, A.J.; Baylin, S.B.; Madzo, J.; Najmanovich, R.; et al. Selective CDK9 Inhibition by Natural Compound Toyocamycin in Cancer Cells. *Cancers* **2022**, *14*, 3340. [[CrossRef](#)]
17. Zhang, H.; Pandey, S.; Travers, M.; Sun, H.; Morton, G.; Madzo, J.; Chung, W.; Khowsathit, J.; Perez-Leal, O.; Barrero, C.A.; et al. Targeting CDK9 Reactivates Epigenetically Silenced Genes in Cancer. *Cell* **2018**, *175*, 1244–1258.e26. [[CrossRef](#)]
18. Huang, C.-H.; Lujambio, A.; Zuber, J.; Tschaharganeh, D.F.; Doran, M.G.; Evans, M.J.; Kitzing, T.; Zhu, N.; de Stanchina, E.; Sawyers, C.L.; et al. CDK9-mediated transcription elongation is required for MYC addiction in hepatocellular carcinoma. *Genes Dev.* **2014**, *28*, 1800–1814. [[CrossRef](#)]
19. Rahaman, M.H.; Kumarasiri, M.; Mekonnen, L.B.; Yu, M.; Diab, S.; Albrecht, H.; Milne, R.W.; Wang, S. Targeting CDK9: A promising therapeutic opportunity in prostate cancer. *Endocr. Relat. Cancer* **2016**, *23*, T211–T226. [[CrossRef](#)]
20. Franco, L.C.; Morales, F.; Boffo, S.; Giordano, A. CDK9: A key player in cancer and other diseases. *J. Cell Biochem.* **2018**, *119*, 1273–1284. [[CrossRef](#)]
21. Gordon, V.; Bhadel, S.; Wunderlich, W.; Zhang, J.; Ficarro, S.B.; Mollah, S.A.; Shabanowitz, J.; Hunt, D.F.; Xenarios, I.; Hahn, W.C.; et al. CDK9 regulates AR promoter selectivity and cell growth through serine 81 phosphorylation. *Mol. Endocrinol.* **2010**, *24*, 2267–2280. [[CrossRef](#)] [[PubMed](#)]
22. Boffo, S.; Damato, A.; Alfano, L.; Giordano, A.; Alfano, L. CDK9 inhibitors in acute myeloid leukemia. *J. Exp. Clin. Cancer Res.* **2018**, *37*, 36. [[CrossRef](#)]
23. Kretz, A.-L.; Schaum, M.; Richter, J.; Kitzig, E.F.; Engler, C.C.; Leithäuser, F.; Henne-Bruns, D.; Knippschild, U.; Lemke, J. CDK9 is a prognostic marker and therapeutic target in pancreatic cancer. *Tumour Biol.* **2017**, *39*, 1010428317694304. [[CrossRef](#)] [[PubMed](#)]
24. Wang, J.; Dean, D.C.; Hornicek, F.J.; Shi, H.; Duan, Z. Cyclin-dependent kinase 9 (CDK9) is a novel prognostic marker and therapeutic target in ovarian cancer. *FASEB J.* **2019**, *33*, 5990–6000. [[CrossRef](#)]
25. Krystof, V.; Baumli, S.; Fürst, R. Perspective of cyclin-dependent kinase 9 (CDK9) as a drug target. *Curr. Pharm. Des.* **2012**, *18*, 2883–2890. [[CrossRef](#)]
26. Mueller, D.; García-Cuellar, M.-P.; Bach, C.; Buhl, S.; Maethner, E.; Slany, R.K. Misguided transcriptional elongation causes mixed lineage leukemia. *PLoS Biol.* **2009**, *7*, e1000249. [[CrossRef](#)]
27. Glaser, S.P.; Lee, E.F.; Trounson, E.; Bouillet, P.; Wei, A.; Fairlie, W.D.; Izon, D.J.; Zuber, J.; Rappaport, A.R.; Herold, M.J.; et al. Anti-apoptotic Mcl-1 is essential for the development and sustained growth of acute myeloid leukemia. *Genes Dev.* **2012**, *26*, 120–125. [[CrossRef](#)]
28. Pawar, A.; Gollavilli, P.N.; Wang, S.; Asangani, I.A. Resistance to BET Inhibitor Leads to Alternative Therapeutic Vulnerabilities in Castration-Resistant Prostate Cancer. *Cell Rep.* **2018**, *22*, 2236–2245. [[CrossRef](#)] [[PubMed](#)]
29. Johnstone, C.N.; Mongroo, P.S.; Rich, A.S.; Schupp, M.; Bowser, M.J.; deLemos, A.S.; Tobias, J.W.; Liu, Y.; Hannigan, G.E.; Rustgi, A.K. Parvin-beta inhibits breast cancer tumorigenicity and promotes CDK9-mediated peroxisome proliferator-activated receptor gamma 1 phosphorylation. *Mol. Cell Biol.* **2008**, *28*, 687–704. [[CrossRef](#)] [[PubMed](#)]
30. Wang, L.; Gao, W.; Hu, F.; Xu, Z.; Wang, F. MicroRNA-874 inhibits cell proliferation and induces apoptosis in human breast cancer by targeting CDK9. *FEBS Lett.* **2014**, *588*, 4527–4535. [[CrossRef](#)]
31. Mitra, P.; Yang, R.-M.; Sutton, J.; Ramsay, R.G.; Gonda, T.J. CDK9 inhibitors selectively target estrogen receptor-positive breast cancer cells through combined inhibition of MYB and MCL-1 expression. *Oncotarget* **2016**, *7*, 9069–9083. [[CrossRef](#)]
32. Kumar, S.K.; LaPlant, B.; Chng, W.J.; Zonder, J.; Callander, N.; Fonseca, R.; Fruth, B.; Roy, V.; Erlichman, C.; Stewart, A.K. Dinaciclib, a novel CDK inhibitor, demonstrates encouraging single-agent activity in patients with relapsed multiple myeloma. *Blood* **2015**, *125*, 443–448. [[CrossRef](#)] [[PubMed](#)]
33. Senderowicz, A.M. Flavopiridol: The first cyclin-dependent kinase inhibitor in human clinical trials. *Investig. N. Drugs* **1999**, *17*, 313–320. [[CrossRef](#)]
34. Walsby, E.; Pratt, G.; Shao, H.; Abbas, A.Y.; Fischer, P.M.; Bradshaw, T.D.; Brennan, P.; Fegan, C.; Wang, S.; Pepper, C. A novel Cdk9 inhibitor preferentially targets tumor cells and synergizes with fludarabine. *Oncotarget* **2014**, *5*, 375–385. [[CrossRef](#)] [[PubMed](#)]
35. Van der Biessen, D.A.; Burger, H.; de Bruijn, P.; Lamers, C.H.J.; Naus, N.; Loferer, H.; Wiemer, E.A.C.; Mathijssen, R.H.J.; de Jonge, M.J.A. Phase I study of RGB-286638, a novel, multitargeted cyclin-dependent kinase inhibitor in patients with solid tumors. *Clin. Cancer Res.* **2014**, *20*, 4776–4783. [[CrossRef](#)]
36. Tong, W.-G.; Chen, R.; Plunkett, W.; Siegel, D.; Sinha, R.; Harvey, R.D.; Badros, A.Z.; Popplewell, L.; Coutre, S.; Fox, J.A.; et al. Phase I and pharmacologic study of SNS-032, a potent and selective Cdk2, 7, and 9 inhibitor, in patients with advanced chronic lymphocytic leukemia and multiple myeloma. *J. Clin. Oncol.* **2010**, *28*, 3015–3022. [[CrossRef](#)] [[PubMed](#)]

37. Cidado, J.; Boiko, S.; Proia, T.; Ferguson, D.; Criscione, S.W.; Martin, M.S.; Pop-Damkov, P.; Su, N.; Franklin, V.N.R.; Chilamakuri, C.S.R.; et al. AZD4573 Is a Highly Selective CDK9 Inhibitor That Suppresses MCL-1 and Induces Apoptosis in Hematologic Cancer Cells. *Clin. Cancer Res.* **2020**, *26*, 922–934. [[CrossRef](#)]
38. McInnes, C. Progress in the evaluation of CDK inhibitors as anti-tumor agents. *Drug Discov. Today* **2008**, *13*, 875–881. [[CrossRef](#)]
39. Zhai, S.; Senderowicz, A.M.; A Sausville, E.; Figg, W.D. Flavopiridol, a novel cyclin-dependent kinase inhibitor, in clinical development. *Ann. Pharmacother.* **2002**, *36*, 905–911. [[CrossRef](#)]
40. Lücking, U.; Scholz, A.; Lienau, P.; Siemeister, G.; Kosemund, D.; Bohlmann, R.; Briem, H.; Terebesi, I.; Meyer, K.; Prella, K.; et al. Identification of Atuveciclib (BAY 1143572), the First Highly Selective, Clinical PTEFb/CDK9 Inhibitor for the Treatment of Cancer. *Chem. Med. Chem.* **2017**, *12*, 1776–1793. [[CrossRef](#)]
41. Di Meo, F.; Fabre, G.; Berka, K.; Ossman, T.; Chantemargue, B.; Palonciová, M.; Marquet, P.; Otyepka, M.; Trouillas, P. In silico pharmacology: Drug membrane partitioning and crossing. *Pharmacol. Res.* **2016**, *111*, 471–486. [[CrossRef](#)] [[PubMed](#)]
42. Ortega, S.S.; Lopez-Cara, L.C.; Salvador, M.K. In silico pharmacology for a multidisciplinary drug discovery process. *Drug Metab. Drug Interact.* **2012**, *27*, 199–207. [[CrossRef](#)] [[PubMed](#)]
43. Ekins, S.; Mestres, J.; Testa, B. In silico pharmacology for drug discovery: Methods for virtual ligand screening and profiling. *Br. J. Pharmacol.* **2007**, *152*, 9–20. [[CrossRef](#)] [[PubMed](#)]
44. Ekins, S.; Mestres, J.; Testa, B. In silico pharmacology for drug discovery: Applications to targets and beyond. *Br. J. Pharmacol.* **2007**, *152*, 21–37. [[CrossRef](#)] [[PubMed](#)]
45. Chakraborty, C.; Priya, D.; Chen, L.; Zhu, H. Evaluating protein-protein interaction (PPI) networks for diseases pathway, target discovery, and drug-design using ‘in silico pharmacology’. *Curr. Protein Pept. Sci.* **2014**, *15*, 561–571. [[CrossRef](#)] [[PubMed](#)]
46. Mestres, J. Computational chemogenomics approaches to systematic knowledge-based drug discovery. *Curr. Opin. Drug Discov. Dev.* **2004**, *7*, 304–313.
47. Pérot, S.; Regad, L.; Reynès, C.; Spérandio, O.; Miteva, M.A.; Villoutreix, B.O.; Camproux, A.-C. Insights into an Original Pocket-Ligand Pair Classification: A Promising Tool for Ligand Profile Prediction. *PLoS ONE* **2013**, *8*, e63730. [[CrossRef](#)]
48. Peng, C.N.H.A.C.J.W.C.H.; Huang, C.; Wang, C. The Anti-Tumor Effect and Mechanisms of Action of Penta-Acetyl Geniposide. *Curr. Cancer Drug Targets* **2005**, *5*, 299–305. [[CrossRef](#)]
49. Cai, L.; Li, C.-M.; Tang, W.-J.; Liu, M.-M.; Chen, W.-N.; Qiu, Y.-Y.; Li, R. Therapeutic Effect of Penta-acetyl Geniposide on Adjuvant-Induced Arthritis in Rats: Involvement of Inducing Synovial Apoptosis and Inhibiting NF- κ B Signal Pathway. *Inflammation* **2018**, *41*, 2184–2195. [[CrossRef](#)]
50. Peng, C.-H.; Tseng, T.-H.; Huang, C.-N.; Hsu, S.-P.; Wang, C.-J. Apoptosis induced by penta-acetyl geniposide in C6 glioma cells is associated with JNK activation and Fas ligand induction. *Toxicol. Appl. Pharmacol.* **2005**, *202*, 172–179. [[CrossRef](#)]
51. Dando, I.; Pacchiana, R.; Pozza, E.D.; Cataldo, I.; Bruno, S.; Conti, P.; Cordani, M.; Grimaldi, A.; Butera, G.; Caraglia, M.; et al. UCP2 inhibition induces ROS/Akt/mTOR axis: Role of GAPDH nuclear translocation in genipin/everolimus anticancer synergism. *Free Radic. Biol. Med.* **2017**, *113*, 176–189. [[CrossRef](#)]
52. Hsu, H.-Y.; Yang, J.-J.; Lin, S.-Y.; Lin, C.-C. Comparisons of geniposidic acid and geniposide on antitumor and radioprotection after sublethal irradiation. *Cancer Lett.* **1997**, *113*, 31–37. [[CrossRef](#)] [[PubMed](#)]
53. Oshima, T.; Sagara, K.; Yoshida, T.; Tong, Y.Y.; Zhang, G.D.; Chen, Y.H. Determination of geniposide, gardenoside, geniposidic acid and genipin-1-beta-gentiobioside in Gardenia jasminoides by high-performance liquid chromatography. *J. Chromatogr.* **1988**, *455*, 410–414. [[CrossRef](#)]
54. Chang, Y.-C.; Tseng, T.-H.; Lee, M.-J.; Hsu, J.-D.; Wang, C.-J. Induction of apoptosis by penta-acetyl geniposide in rat C6 glioma cells. *Chem. Interact.* **2002**, *141*, 243–257. [[CrossRef](#)] [[PubMed](#)]
55. Peng, C.-H.; Huang, C.-N.; Hsu, S.-P.; Wang, C.-J. Penta-acetyl geniposide-induced apoptosis involving transcription of NGF/p75 via MAPK-mediated AP-1 activation in C6 glioma cells. *Toxicology* **2007**, *238*, 130–139. [[CrossRef](#)] [[PubMed](#)]
56. Wang, C.J.; Tseng, T.H.; Lin, J.K. Penta-acetyl geniposide: Isolation, identification and primary effect on C6 glioma cells in vitro. *Anticancer Res.* **1992**, *12*, 911–915.
57. Peng, C.H.; Peng, C.-H.; Huang, C.-N.; Hsu, S.-P.; Wang, C.-J. Penta-acetyl geniposide induce apoptosis in C6 glioma cells by modulating the activation of neutral sphingomyelinase-induced p75 nerve growth factor receptor and protein kinase Cdelta pathway. *Mol. Pharmacol.* **2006**, *70*, 997–1004. [[CrossRef](#)] [[PubMed](#)]
58. Habtemariam, S.; Lentini, G. Plant-Derived Anticancer Agents: Lessons from the Pharmacology of Geniposide and Its Aglycone, Genipin. *Biomedicines* **2018**, *6*, 39. [[CrossRef](#)]
59. Rauf, A.; Imran, M.; Khan, I.A.; Ur-Rehman, M.; Gilani, S.A.; Mehmood, Z.; Mubarak, M.S. Anticancer potential of quercetin: A comprehensive review. *Phytother. Res.* **2018**, *32*, 2109–2130. [[CrossRef](#)]
60. Davoodvandi, A.; Varkani, M.S.; Clark, C.C.T.; Jafarnejad, S. Quercetin as an anticancer agent: Focus on esophageal cancer. *J. Food Biochem.* **2020**, *44*, e13374. [[CrossRef](#)]
61. Niedzwiecki, A.; Roomi, M.W.; Kalinovsky, T.; Rath, M. Anticancer Efficacy of Polyphenols and Their Combinations. *Nutrients* **2016**, *8*, 552. [[CrossRef](#)] [[PubMed](#)]
62. Soofiyani, S.R.; Hosseini, K.; Forouhandeh, H.; Ghasemnejad, T.; Tarhriz, V.; Asgharian, P.; Reiner, Ž.; Sharifi-Rad, J.; Cho, W.C. Quercetin as a Novel Therapeutic Approach for Lymphoma. *Oxid. Med. Cell Longev.* **2021**, *2021*, 3157867. [[CrossRef](#)] [[PubMed](#)]

63. Hashemzaei, M.; Delarami Far, A.; Yari, A.; Heravi, R.E.; Tabrizian, K.; Taghdisi, S.M.; Sadegh, S.E.; Tsarouhas, K.; Kouretas, D.; Tzanakakis, G.; et al. Anticancer and apoptosis-inducing effects of quercetin in vitro and in vivo. *Oncol. Rep.* **2017**, *38*, 819–828. [[CrossRef](#)] [[PubMed](#)]
64. Vinayak, M.; Maurya, A.K. Quercetin Loaded Nanoparticles in Targeting Cancer: Recent Development. *Anti Cancer Agents Med. Chem.* **2019**, *19*, 1560–1576. [[CrossRef](#)]
65. Reyes-Farias, M.; Carrasco-Pozo, C. The Anti-Cancer Effect of Quercetin: Molecular Implications in Cancer Metabolism. *Int. J. Mol. Sci.* **2019**, *20*, 3177. [[CrossRef](#)]
66. Hosseini, A.; Razavi, B.M.; Banach, M.; Hosseinzadeh, H. Quercetin and metabolic syndrome: A review. *Phytotherapy Res.* **2021**, *35*, 5352–5364. [[CrossRef](#)]
67. Czerwonka, A.; Maciolek, U.; Kalafut, J.; Mendyk, E.; Kuzniar, A.; Rzeski, W. Anticancer effects of sodium and potassium quercetin-5'-sulfonates through inhibition of proliferation, induction of apoptosis, and cell cycle arrest in the HT-29 human adenocarcinoma cell line. *Bioorg. Chem.* **2020**, *94*, 103426. [[CrossRef](#)]
68. Shafabakhsh, R.; Asemi, Z. Quercetin: A natural compound for ovarian cancer treatment. *J. Ovar. Res.* **2019**, *12*, 55. [[CrossRef](#)]
69. Massi, A.; Bortolini, O.; Ragno, D.; Bernardi, T.; Sacchetti, G.; Tacchini, M.; De Risi, C. Research Progress in the Modification of Quercetin Leading to Anticancer Agents. *Molecules* **2017**, *22*, 1270. [[CrossRef](#)]
70. Tang, S.-M.; Deng, X.-T.; Zhou, J.; Li, Q.-P.; Ge, X.-X.; Miao, L. Pharmacological basis and new insights of quercetin action in respect to its anti-cancer effects. *Biomed. Pharmacother.* **2019**, *121*, 109604. [[CrossRef](#)]
71. Wang, Z.; Ma, J.; Li, X.; Wu, Y.; Shi, H.; Chen, Y.; Lu, G.; Shen, H.; Lu, G.; Zhou, J. Quercetin induces p53-independent cancer cell death through lysosome activation by the transcription factor EB and Reactive Oxygen Species-dependent ferroptosis. *Br. J. Pharmacol.* **2020**, *178*, 1133–1148. [[CrossRef](#)]
72. Giordano, A.; Tommonaro, G. Curcumin and Cancer. *Nutrients* **2019**, *11*, 2376. [[CrossRef](#)]
73. Joshi, P.; Joshi, S.; Semwal, D.; Bisht, A.; Paliwal, S.; Dwivedi, J.; Sharma, S. Curcumin: An Insight into Molecular Pathways Involved in Anticancer Activity. *Mini-Reviews Med. Chem.* **2021**, *21*, 2420–2457. [[CrossRef](#)] [[PubMed](#)]
74. Unlu, A.; Nayir, E.; Kalenderoglu, M.D.; Kirca, O.; Ozdogan, M. Curcumin (Turmeric) and cancer. *J. BUON* **2016**, *21*, 1050–1060. [[PubMed](#)]
75. Zia, A.; Farkhondeh, T.; Pourbagher-Shahri, A.M.; Samarghandian, S. The role of curcumin in aging and senescence: Molecular mechanisms. *Biomed. Pharmacother.* **2021**, *134*, 111119. [[CrossRef](#)]
76. Kunnumakkara, A.B.; Bordoloi, D.; Harsha, C.; Banik, K.; Gupta, S.C.; Aggarwal, B.B. Curcumin mediates anticancer effects by modulating multiple cell signaling pathways. *Clin. Sci.* **2017**, *131*, 1781–1799. [[CrossRef](#)] [[PubMed](#)]
77. Rodrigues, F.C.; Kumar, N.A.; Thakur, G. Developments in the anticancer activity of structurally modified curcumin: An up-to-date review. *Eur. J. Med. Chem.* **2019**, *177*, 76–104. [[CrossRef](#)]
78. Allegra, A.; Innao, V.; Russo, S.; Gerace, D.; Alonci, A.; Musolino, C. Anticancer Activity of Curcumin and Its Analogues: Preclinical and Clinical Studies. *Cancer Investig.* **2017**, *35*, 1–22. [[CrossRef](#)]
79. Hassanalilou, T.; Ghavamzadeh, S.; Khalili, L. Curcumin and Gastric Cancer: A Review on Mechanisms of Action. *J. Gastrointest. Cancer* **2019**, *50*, 185–192. [[CrossRef](#)]
80. Tomeh, M.A.; Hadianamrei, R.; Zhao, X. A Review of Curcumin and Its Derivatives as Anticancer Agents. *Int. J. Mol. Sci.* **2019**, *20*, 1033. [[CrossRef](#)]
81. Kotha, R.R.; Luthria, D.L. Curcumin: Biological, Pharmaceutical, Nutraceutical, and Analytical Aspects. *Molecules* **2019**, *24*, 2930. [[CrossRef](#)]
82. Wong, S.; Kamarudin, M.; Naidu, R. Anticancer Mechanism of Curcumin on Human Glioblastoma. *Nutrients* **2021**, *13*, 950. [[CrossRef](#)]
83. Wang, Y.; Yu, J.; Cui, R.; Lin, J.; Ding, X. Curcumin in Treating Breast Cancer: A Review. *J. Lab. Autom.* **2016**, *21*, 723–731. [[CrossRef](#)]
84. Mbese, Z.; Khwaza, V.; Aderibigbe, B.A. Curcumin and Its Derivatives as Potential Therapeutic Agents in Prostate, Colon and Breast Cancers. *Molecules* **2019**, *24*, 4386. [[CrossRef](#)]
85. Yu, T.-J.; Tang, J.-Y.; Lin, L.-C.; Lien, W.-J.; Cheng, Y.-B.; Chang, F.-R.; Ou-Yang, F.; Chang, H.-W. Withanolide C Inhibits Proliferation of Breast Cancer Cells via Oxidative Stress-Mediated Apoptosis and DNA Damage. *Antioxidants* **2020**, *9*, 873. [[CrossRef](#)]
86. Xu, Q.Q.; Wang, K.W. Natural Bioactive New Withanolides. *Mini Rev. Med. Chem.* **2020**, *20*, 1101–1117. [[CrossRef](#)] [[PubMed](#)]
87. Huang, M.; He, J.-X.; Hu, H.-X.; Zhang, K.; Wang, X.-N.; Zhao, B.-B.; Lou, H.-X.; Ren, D.-M.; Shen, T. Withanolides from the genus *Physalis*: A review on their phytochemical and pharmacological aspects. *J. Pharm. Pharmacol.* **2020**, *72*, 649–669. [[CrossRef](#)]
88. Tang, J.-Y.; Cheng, Y.-B.; Chuang, Y.-T.; Yang, K.-H.; Chang, F.-R.; Liu, W.; Chang, H.-W. Oxidative Stress and AKT-Associated Angiogenesis in a Zebrafish Model and Its Potential Application for Withanolides. *Cells* **2022**, *11*, 961. [[CrossRef](#)]
89. Xia, G.Y.; Cao, S.-J.; Chen, L.-X.; Qiu, F. Natural withanolides, an update. *Nat. Prod. Rep.* **2022**, *39*, 784–813. [[CrossRef](#)]
90. Xiang, K.; Li, C.; Li, M.-X.; Song, Z.-R.; Ma, X.-X.; Sun, D.-J.; Li, H.; Chen, L.-X. Withanolides isolated from *Tubocapsicum anomalum* and their antiproliferative activity. *Bioorg. Chem.* **2021**, *110*, 104809. [[CrossRef](#)] [[PubMed](#)]
91. Liu, W.; Huang, S.; Chen, Z.; Wang, H.; Wu, H.; Zhang, D. Temsirolimus, the mTOR inhibitor, induces autophagy in adenoid cystic carcinoma: In vitro and in vivo. *Pathol. Res. Pract.* **2014**, *210*, 764–769. [[CrossRef](#)] [[PubMed](#)]

92. Berman, H.M.; Westbrook, J.; Feng, Z.; Gilliland, G.; Bhat, T.N.; Weissig, H.; Shindyalov, I.N.; Bourne, P.E. The Protein Data Bank. *Nucleic Acids Res.* **2000**, *28*, 235–242. [[CrossRef](#)] [[PubMed](#)]
93. Sastry, G.M.; Adzhigirey, M.; Day, T.; Annabhimoju, R.; Sherman, W. Protein and ligand preparation: Parameters, protocols, and influence on virtual screening enrichments. *J. Comput. Aided Mol. Des.* **2013**, *27*, 221–234. [[CrossRef](#)] [[PubMed](#)]
94. Shelley, J.C.; Cholleti, A.; Frye, L.L.; Greenwood, J.R.; Timlin, M.R.; Uchimaya, M. Epik: A software program for pK_a prediction and protonation state generation for drug-like molecules. *J. Comput. Mol. Des.* **2007**, *21*, 681–691. [[CrossRef](#)]
95. Harder, E.; Damm, W.; Maple, J.; Wu, C.; Reboul, M.; Xiang, J.Y.; Wang, L.; Lupyan, D.; Dahlgren, M.K.; Knight, J.L.; et al. OPLS3: A Force Field Providing Broad Coverage of Drug-like Small Molecules and Proteins. *J. Chem. Theory Comput.* **2016**, *12*, 281–296. [[CrossRef](#)]
96. Kim, S.; Thiessen, P.A.; Bolton, E.E.; Chen, J.; Fu, G.; Gindulyte, A.; Han, L.; He, J.; He, S.; Shoemaker, B.A.; et al. PubChem substance and compound databases. *Nucleic Acids Res.* **2016**, *44*, D1202–D1213. [[CrossRef](#)] [[PubMed](#)]
97. Friesner, R.A.; Murphy, R.B.; Repasky, M.P.; Frye, L.L.; Greenwood, J.R.; Halgren, T.A.; Sanschagrin, P.C.; Mainz, D.T. Extra Precision Glide: Docking and Scoring Incorporating a Model of Hydrophobic Enclosure for Protein–Ligand Complexes. *J. Med. Chem.* **2006**, *49*, 6177–6196. [[CrossRef](#)]
98. Perola, E.; Walters, W.P.; Charifson, P.S. A detailed comparison of current docking and scoring methods on systems of pharmaceutical relevance. *Proteins Struct. Funct. Bioinform.* **2004**, *56*, 235–249. [[CrossRef](#)]
99. Norinder, U.; Bergström, C.A. Prediction of ADMET Properties. *Chem. Med. Chem.* **2006**, *1*, 920–937. [[CrossRef](#)]
100. Daina, A.; Michielin, O.; Zoete, V. SwissADME: A free web tool to evaluate pharmacokinetics, drug-likeness and medicinal chemistry friendliness of small molecules. *Sci. Rep.* **2017**, *7*, 42717. [[CrossRef](#)]
101. Pires, D.E.V.; Blundell, T.L.; Ascher, D.B. pkCSM: Predicting Small-Molecule Pharmacokinetic and Toxicity Properties Using Graph-Based Signatures. *J. Med. Chem.* **2015**, *58*, 4066–4072. [[CrossRef](#)]
102. Abraham, M.J.; Murtola, T.; Schulz, R.; Páll, S.; Smith, J.C.; Hess, B.; Lindahl, E. GROMACS: High performance molecular simulations through multi-level parallelism from laptops to supercomputers. *SoftwareX* **2015**, *1–2*, 19–25. [[CrossRef](#)]
103. Bjelkmar, P.; Larsson, P.; Cuendet, M.A.; Hess, B.; Lindahl, E. Implementation of the CHARMM Force Field in GROMACS: Analysis of Protein Stability Effects from Correction Maps, Virtual Interaction Sites, and Water Models. *J. Chem. Theory Comput.* **2010**, *6*, 459–466. [[CrossRef](#)]
104. Khafaji, K.A.; Tok, T.T. Amygdalin as multi-target anticancer drug against targets of cell division cycle: Double docking and molecular dynamics simulation. *J. Biomol. Struct. Dyn.* **2020**, *39*, 1965–1974. [[CrossRef](#)]
105. Essmann, U.; Perera, L.; Berkowitz, M.L.; Darden, T.; Lee, H.; Pedersen, L.G. A smooth particle mesh Ewald method. *J. Chem. Phys.* **1995**, *103*, 8577–8593. [[CrossRef](#)]
106. Hess, U.; Blairy, S.; Kleck, R.E. The Intensity of Emotional Facial Expressions and Decoding Accuracy. *J. Nonverbal Behav.* **1997**, *21*, 241–257. [[CrossRef](#)]
107. Gfeller, D.; Grosdidier, A.; Wirth, M.; Daina, A.; Michielin, O.; Zoete, V. SwissTargetPrediction: A web server for target prediction of bioactive small molecules. *Nucleic Acids Res.* **2014**, *42*, W32–W38. [[CrossRef](#)]
108. Khan, R.A.; Hossain, R.; Siyadatpanah, A.; Al-Khafaji, K.; Khalipha, A.B.R.; Dey, D.; Asha, U.H.; Biswas, P.; Saikat, A.S.M.; Chenari, H.A.; et al. Diterpenes/Diterpenoids and Their Derivatives as Potential Bioactive Leads against Dengue Virus: A Computational and Network Pharmacology Study. *Molecules* **2021**, *26*, 6821. [[CrossRef](#)]
109. Szklarczyk, D.; Gable, A.L.; Nastou, K.C.; Lyon, D.; Kirch, R.; Pyysalo, S.; Doncheva, N.T.; Legeay, M.; Fang, T.; Bork, P.; et al. The STRING database in 2021: Customizable protein-protein networks, and functional characterization of user-uploaded gene/measurement sets. *Nucleic Acids Res.* **2021**, *49*, D605–D612. [[CrossRef](#)]
110. Doncheva, N.T.; Morris, J.H.; Gorodkin, J.; Jensen, L.J. Cytoscape StringApp: Network Analysis and Visualization of Proteomics Data. *J. Proteome Res.* **2019**, *18*, 623–632. [[CrossRef](#)]
111. Shannon, P.; Markiel, A.; Ozier, O.; Baliga, N.S.; Wang, J.T.; Ramage, D.; Amin, N.; Schwikowski, B.; Ideker, T. Cytoscape: A software environment for integrated models of Biomolecular Interaction Networks. *Genome Res.* **2003**, *13*, 2498–2504. [[CrossRef](#)]
112. Sheik, S.; Sundararajan, P.; Hussain, A.; Sekar, K. Ramachandran plot on the web. *Bioinformatics* **2002**, *18*, 1548–1549. [[CrossRef](#)]
113. Pinzi, L.; Rastelli, G. Molecular Docking: Shifting Paradigms in Drug Discovery. *Int. J. Mol. Sci.* **2019**, *20*, 4331. [[CrossRef](#)]
114. Saikat, A.S.M. An In Silico Approach for Potential Natural Compounds as Inhibitors of Protein CDK1/Cks2. *Chem. Proc.* **2022**, *8*, 5.
115. Saikat, A.S.M.; Uddin, E.; Ahmad, T.; Mahmud, S.; Imran, A.S.; Ahmed, S.; Alyami, S.A.; Moni, M.A. Structural and Functional Elucidation of IF-3 Protein of *Chloroflexus aurantiacus* Involved in Protein Biosynthesis: An In Silico Approach. *BioMed Res. Int.* **2021**, *2021*, 9050026. [[CrossRef](#)]
116. Kaur, T.; Madgulkar, A.; Bhalekar, M.; Asgaonkar, K.; Marwaha, T.K. Molecular Docking in Formulation and Development. *Curr. Cancer Drug Targets* **2019**, *16*, 30–39. [[CrossRef](#)]
117. Saikat, A.S.M.; Islam, R.; Mahmud, S.; Imran, M.A.S.; Alam, M.S.; Masud, M.H.; Uddin, M.E. Structural and Functional Annotation of Uncharacterized Protein NCGM946K2_146 of *Mycobacterium Tuberculosis*: An In-Silico Approach. *Proceedings* **2020**, *66*, 13.
118. Ferreira, L.G.; Dos Santos, R.N.; Oliva, G.; Andricopulo, A.D. Molecular Docking and Structure-Based Drug Design Strategies. *Molecules* **2015**, *20*, 13384–13421. [[CrossRef](#)]
119. Sulimov, V.B.; Kutov, D.C.; Sulimov, A.V. Advances in Docking. *Curr. Med. Chem.* **2019**, *26*, 7555–7580. [[CrossRef](#)]

120. Ferreira, L.L.; Andricopulo, A.D. ADMET modeling approaches in drug discovery. *Drug Discov. Today* **2019**, *24*, 1157–1165. [[CrossRef](#)]
121. Daina, A.; Michielin, O.; Zoete, V. iLOGP: A simple, robust, and efficient description of n-octanol/water partition coefficient for drug design using the GB/SA approach. *J. Chem. Inf. Model* **2014**, *54*, 3284–3301. [[CrossRef](#)]
122. Daina, A.; Zoete, V. A BOILED-Egg To Predict Gastrointestinal Absorption and Brain Penetration of Small Molecules. *Chem. Med. Chem.* **2016**, *11*, 1117–1121. [[CrossRef](#)]
123. Kar, S.; Leszczynski, J. Open access in silico tools to predict the ADMET profiling of drug candidates. *Expert Opin. Drug Discov.* **2020**, *15*, 1473–1487. [[CrossRef](#)] [[PubMed](#)]
124. Arnott, J.A.; Planey, S.L. The influence of lipophilicity in drug discovery and design. *Expert Opin. Drug Discov.* **2012**, *7*, 863–875. [[CrossRef](#)]
125. Psimadas, D.; Georgoulas, P.; Valotassiou, V.; Loudos, G. Molecular Nanomedicine Towards Cancer: 111In-Labeled Nanoparticles. *J. Pharm. Sci.* **2012**, *101*, 2271–2280. [[CrossRef](#)]
126. Bruno, C.D.; Harmatz, J.S.; Duan, S.X.; Zhang, Q.; Chow, C.R.; Greenblatt, D.J. Effect of lipophilicity on drug distribution and elimination: Influence of obesity. *Br. J. Clin. Pharmacol.* **2021**, *87*, 3197–3205. [[CrossRef](#)] [[PubMed](#)]
127. Yilancioglu, K.; Weinstein, Z.B.; Meydan, C.; Akhmetov, A.; Toprak, I.; Durmaz, A.; Iossifov, I.; Kazan, H.; Roth, F.P.; Cokol, M. Target-Independent Prediction of Drug Synergies Using Only Drug Lipophilicity. *J. Chem. Inf. Model.* **2014**, *54*, 2286–2293. [[CrossRef](#)]
128. Paneth, A.; Hawrył, A.; Plech, T.; Hawrył, M.; Świeboda, R.; Janowska, D.; Wujec, M.; Paneth, P. Lipophilicity Studies on Thiosemicarbazide Derivatives. *Molecules* **2017**, *22*, 952. [[CrossRef](#)]
129. Van der Spoel, D.; Manzetti, S.; Zhang, H.; Klamt, A. Prediction of Partition Coefficients of Environmental Toxins Using Computational Chemistry Methods. *ACS Omega* **2019**, *4*, 13772–13781. [[CrossRef](#)]
130. Ritchie, T.J.; Macdonald, S.J.F.; Peace, S.; Pickett, S.D.; Luscombe, C.N. Increasing small molecule drug developability in sub-optimal chemical space. *Med. Chem. Comm.* **2013**, *4*, 673–680. [[CrossRef](#)]
131. Savjani, K.T.; Gajjar, A.K.; Savjani, J.K. Drug solubility: Importance and enhancement techniques. *ISRN Pharm.* **2012**, *2012*, 195727. [[CrossRef](#)] [[PubMed](#)]
132. Ottaviani, G.; Gosling, D.J.; Patissier, C.; Rodde, S.; Zhou, L.; Faller, B. What is modulating solubility in simulated intestinal fluids? *Eur. J. Pharm. Sci.* **2010**, *41*, 452–457. [[CrossRef](#)] [[PubMed](#)]
133. Delaney, J.S. ESOL: Estimating Aqueous Solubility Directly from Molecular Structure. *J. Chem. Inf. Comput. Sci.* **2004**, *44*, 1000–1005. [[CrossRef](#)]
134. Turfus, S.; Delgoda, R.; Picking, D.; Gurley, B.J. *Chapter 25—Pharmacokinetics*; Academic Press: Boston, MA, USA, 2017; pp. 495–512.
135. Saghir, S.A.; Ansari, R.A. *Pharmacokinetics, in Reference Module in Biomedical Sciences*; Elsevier: Amsterdam, The Netherlands, 2018.
136. Waller, D.G.; Sampson, A.P. 2-Pharmacokinetics. In *Medical Pharmacology and Therapeutics*, 5th ed.; Waller, D.G., Sampson, A.P., Eds.; Elsevier: Amsterdam, The Netherlands, 2018; pp. 33–62.
137. Paixão, P.; Gouveia, L.F.; Morais, J.A. Prediction of the human oral bioavailability by using in vitro and in silico drug related parameters in a physiologically based absorption model. *Int. J. Pharm.* **2012**, *429*, 84–98. [[CrossRef](#)]
138. Wu, X.-X.; Huang, X.-L.; Chen, R.-R.; Li, T.; Ye, H.-J.; Xie, W.; Huang, Z.-M.; Cao, G.-Z. Paeoniflorin Prevents Intestinal Barrier Disruption and Inhibits Lipopolysaccharide (LPS)-Induced Inflammation in Caco-2 Cell Monolayers. *Inflammation* **2019**, *42*, 2215–2225. [[CrossRef](#)] [[PubMed](#)]
139. Henri, J.; Lancelleur, R.; Delmas, J.-M.; Fessard, V.; Huguet, A. Permeability of the Cyanotoxin Microcystin-RR across a Caco-2 Cells Monolayer. *Toxins* **2021**, *13*, 178. [[CrossRef](#)]
140. Vincze, A.; Dargó, G.; Rácz, A.; Balogh, G.T. A corneal-PAMPA-based in silico model for predicting corneal permeability. *J. Pharm. Biomed. Anal.* **2021**, *203*, 114218. [[CrossRef](#)] [[PubMed](#)]
141. Angelis, I.D.; Turco, L. Caco-2 cells as a model for intestinal absorption. *Curr. Protoc. Toxicol.* **2011**, *47*, 20.6.1–20.6.15. [[CrossRef](#)]
142. Volpe, D.A. Drug-permeability and transporter assays in Caco-2 and MDCK cell lines. *Future Med. Chem.* **2011**, *3*, 2063–2077. [[CrossRef](#)]
143. Drago, S.; El Asmar, R.; Di Pierro, M.; Grazia Clemente, M.; Tripathi, A.; Sapone, A.; Thakar, M.; Iacono, G.; Carroccio, A.; D’Agate, C.; et al. Gliadin, zonulin and gut permeability: Effects on celiac and non-celiac intestinal mucosa and intestinal cell lines. *Scand J. Gastroenterol.* **2006**, *41*, 408–419. [[CrossRef](#)]
144. Volpe, D.A. Advances in cell-based permeability assays to screen drugs for intestinal absorption. *Expert Opin. Drug Discov.* **2020**, *15*, 539–549. [[CrossRef](#)]
145. Le Roux, A.; Blaise, E.; Boudreault, P.-L.; Comeau, C.; Doucet, A.; Giarrusso, M.; Collin, M.-P.; Neubauer, T.; Koelling, F.; Göller, A.H.; et al. Structure–Permeability Relationship of Semipeptidic Macrocycles—Understanding and Optimizing Passive Permeability and Efflux Ratio. *J. Med. Chem.* **2020**, *63*, 6774–6783. [[CrossRef](#)]
146. Toutain, P.L.; Bousquet-Mélou, A. Plasma clearance. *J. Vet Pharmacol. Ther.* **2004**, *27*, 415–425. [[CrossRef](#)]
147. Roth, R.A.; Wiersma, D.A. Role of the Lung in Total Body Clearance of Circulating Drugs. *Clin. Pharmacokinet.* **1979**, *4*, 355–367. [[CrossRef](#)]

148. Pippa, L.F.; de Oliveira, M.L.; Rocha, A.; de Andrade, J.M.; Lanchote, V.L. Total, renal and hepatic clearances of doxorubicin and formation clearance of doxorubicinol in patients with breast cancer: Estimation of doxorubicin hepatic extraction ratio. *J. Pharm. Biomed. Anal.* **2020**, *185*, 113231. [[CrossRef](#)]
149. Mathialagan, S.; Piotrowski, M.A.; Tess, D.A.; Feng, B.; Litchfield, J.; Varma, M.V. Quantitative Prediction of Human Renal Clearance and Drug-Drug Interactions of Organic Anion Transporter Substrates Using In Vitro Transport Data: A Relative Activity Factor Approach. *Drug Metab. Dispos.* **2017**, *45*, 409–417. [[CrossRef](#)]
150. Harrison, J.; de Bruyn, T.; Darwich, A.S.; Houston, J.B. Simultaneous Assessment In Vitro of Transporter and Metabolic Processes in Hepatic Drug Clearance: Use of a Media Loss Approach. *Drug Metab. Dispos.* **2018**, *46*, 405–414. [[CrossRef](#)]
151. Shitara, Y.; Maeda, K.; Ikejiri, K.; Yoshida, K.; Horie, T.; Sugiyama, Y. Clinical significance of organic anion transporting polypeptides (OATPs) in drug disposition: Their roles in hepatic clearance and intestinal absorption. *Biopharm. Drug Dispos.* **2013**, *34*, 45–78. [[CrossRef](#)]
152. Soulières, D.; Gelmon, K.A. Sotorasib: Is Maximum Tolerated Dose Really the Issue at Hand? *J. Clin. Oncol.* **2021**, *39*, 3427–3429. [[CrossRef](#)]
153. Stampfer, H.G.; Gabb, G.M.; Dimmitt, S.B. Why maximum tolerated dose? *Br. J. Clin. Pharmacol.* **2019**, *85*, 2213–2217. [[CrossRef](#)]
154. Bozkurt, B. Target Dose Versus Maximum Tolerated Dose in Heart Failure: Time to Calibrate and Define Actionable Goals. *JACC Heart Fail* **2019**, *7*, 359–362. [[CrossRef](#)]
155. Kojima, M. Adaptive design for identifying maximum tolerated dose early to accelerate dose-finding trial. *BMC Med. Res. Methodol.* **2022**, *22*, 97. [[CrossRef](#)]
156. Gad, S.C. LD50/LC50 (Lethal Dosage 50/Lethal Concentration 50). In *Encyclopedia of Toxicology*, 3rd ed.; Wexler, P., Ed.; Academic Press: Cambridge, MA, USA, 2014; pp. 58–60.
157. Aucar, M.G.; Cavalotto, C.N. Molecular Docking Using Quantum Mechanical-Based Methods. *Methods Mol. Biol.* **2020**, *2114*, 269–284.
158. Cavalotto, C.; Aucar, M.G. High-Throughput Docking Using Quantum Mechanical Scoring. *Front. Chem.* **2020**, *8*, 246. [[CrossRef](#)]
159. Li, J.; Fu, A.; Zhang, L. An Overview of Scoring Functions Used for Protein–Ligand Interactions in Molecular Docking. *Interdiscip. Sci. Comput. Life Sci.* **2019**, *11*, 320–328. [[CrossRef](#)]
160. Kassel, D.B. Applications of high-throughput ADME in drug discovery. *Curr. Opin. Chem. Biol.* **2004**, *8*, 339–345. [[CrossRef](#)]
161. Wang, J.; Skolnik, S. Recent Advances in Physicochemical and ADMET Profiling in Drug Discovery. *Chem. Biodivers.* **2009**, *6*, 1887–1899. [[CrossRef](#)]
162. Cheng, F.; Li, W.; Liu, G.; Tang, Y. In Silico ADMET Prediction: Recent Advances, Current Challenges and Future Trends. *Curr. Top. Med. Chem.* **2013**, *13*, 1273–1289. [[CrossRef](#)]
163. Van de Waterbeemd, H. Improving compound quality through in vitro and in silico physicochemical profiling. *Chem. Biodivers.* **2009**, *6*, 1760–1766. [[CrossRef](#)]
164. Cruciani, G.; Milletti, F.; Storch, L.; Sforza, G.; Goracci, L. ChemInform Abstract: In silico pKa Prediction and ADMET Profiling. *ChemInform* **2010**, *6*, 1812–1821. [[CrossRef](#)]
165. Lipinski, C.A. Lead- and drug-like compounds: The rule-of-five revolution. *Drug Discov. Today Technol.* **2004**, *1*, 337–341. [[CrossRef](#)]
166. Prasanna, S.; Doerksen, R.J. Topological polar surface area: A useful descriptor in 2D-QSAR. *Curr. Med. Chem.* **2009**, *16*, 21–41. [[CrossRef](#)]
167. Fernandes, J.; Gattass, C.R. Topological polar surface area defines substrate transport by multidrug resistance associated protein 1 (MRP1/ABCC1). *J. Med. Chem.* **2009**, *52*, 1214–1218. [[CrossRef](#)]
168. Pajouhesh, H.; Lenz, G.R. Medicinal chemical properties of successful central nervous system drugs. *NeuroRX* **2005**, *2*, 541–553. [[CrossRef](#)]
169. Hitchcock, S.A.; Pennington, L.D. Structure–Brain Exposure Relationships. *J. Med. Chem.* **2006**, *49*, 7559–7583. [[CrossRef](#)]
170. Jia, C.-Y.; Li, J.-Y.; Hao, G.-F.; Yang, G.-F. A drug-likeness toolbox facilitates ADMET study in drug discovery. *Drug Discov. Today* **2019**, *25*, 248–258. [[CrossRef](#)]
171. Jorgensen, W.L.; Duffy, E.M. Prediction of drug solubility from structure. *Adv. Drug Deliv. Rev.* **2002**, *54*, 355–366. [[CrossRef](#)] [[PubMed](#)]
172. Augustijns, P.; Wuyts, B.; Hens, B.; Annaert, P.; Butler, J.; Brouwers, J. A review of drug solubility in human intestinal fluids: Implications for the prediction of oral absorption. *Eur. J. Pharm. Sci.* **2014**, *57*, 322–332. [[CrossRef](#)] [[PubMed](#)]
173. Cheng, T.; Zhao, Y.; Li, X.; Lin, F.; Xu, Y.; Zhang, X.; Li, A.Y.; Wang, R.; Lai, L. Computation of Octanol–Water Partition Coefficients by Guiding an Additive Model with Knowledge. *J. Chem. Inf. Model.* **2007**, *47*, 2140–2148. [[CrossRef](#)]
174. Zhang, Y. Overview of Transporters in Pharmacokinetics and Drug Discovery. *Curr. Protoc. Pharmacol.* **2018**, *82*, e46. [[CrossRef](#)]
175. Reichel, A.; Lienau, P. Pharmacokinetics in Drug Discovery: An Exposure-Centred Approach to Optimising and Predicting Drug Efficacy and Safety. *Handb. Exp. Pharmacol.* **2016**, *232*, 235–260.
176. Glassman, P.M.; Balthasar, J.P. Physiologically-based modeling of monoclonal antibody pharmacokinetics in drug discovery and development. *Drug Metab. Pharmacokinet.* **2019**, *34*, 3–13. [[CrossRef](#)]
177. Montanari, F.; Ecker, G.F. Prediction of drug-ABC-transporter interaction—Recent advances and future challenges. *Adv. Drug Deliv. Rev.* **2015**, *86*, 17–26. [[CrossRef](#)]

178. Seelig, A. P-Glycoprotein: One Mechanism, Many Tasks and the Consequences for Pharmacotherapy of Cancers. *Front Oncol.* **2020**, *10*, 576559. [[CrossRef](#)] [[PubMed](#)]
179. Yew, W.W.; Chang, K.C.; Chan, D.P. Oxidative Stress and First-Line Antituberculosis Drug-Induced Hepatotoxicity. *Antimicrob. Agents Chemother.* **2018**, *62*, e02637-17. [[CrossRef](#)]
180. Chang, C.Y.; Schiano, T.D. Review article: Drug hepatotoxicity. *Aliment. Pharmacol. Ther.* **2007**, *25*, 1135–1151. [[CrossRef](#)]
181. Murray, K.F.; Hadzic, N.; Wirth, S.; Bassett, M.; Kelly, D. Drug-related Hepatotoxicity and Acute Liver Failure. *J. Pediatr. Gastroenterol. Nutr.* **2008**, *47*, 395–405. [[CrossRef](#)]
182. Liu, X.; Shi, D.; Zhou, S.; Liu, H.; Liu, H.; Yao, X. Molecular dynamics simulations and novel drug discovery. *Expert Opin. Drug Discov.* **2018**, *13*, 23–37. [[CrossRef](#)]
183. Saikia, S.; Bordoloi, M. Molecular Docking: Challenges, Advances and its Use in Drug Discovery Perspective. *Curr. Drug Targets* **2019**, *20*, 501–521. [[CrossRef](#)]
184. Śledź, P.; Cafilisch, A. Protein structure-based drug design: From docking to molecular dynamics. *Curr. Opin. Struct. Biol.* **2018**, *48*, 93–102. [[CrossRef](#)]
185. Guilbert, C.; James, T.L. Docking to RNA via Root-Mean-Square-Deviation-Driven Energy Minimization with Flexible Ligands and Flexible Targets. *J. Chem. Inf. Model.* **2008**, *48*, 1257–1268. [[CrossRef](#)]
186. Rout, A.K.; Barnwal, R.P.; Agarwal, G.; Chary, K.V.R. Root-mean-square-deviation-based rapid backbone resonance assignments in proteins. *Org. Magn. Reson.* **2010**, *48*, 793–797. [[CrossRef](#)] [[PubMed](#)]
187. Harada, R.; Shigeta, Y. Temperature-Shuffled Structural Dissimilarity Sampling Based on a Root-Mean-Square Deviation. *J. Chem. Inf. Model.* **2018**, *58*, 1397–1405. [[CrossRef](#)] [[PubMed](#)]
188. Cazals, F.; Tetley, R. Characterizing molecular flexibility by combining least root mean square deviation measures. *Proteins: Struct. Funct. Bioinform.* **2019**, *87*, 380–389. [[CrossRef](#)]
189. Pitera, J.W. Expected Distributions of Root-Mean-Square Positional Deviations in Proteins. *J. Phys. Chem. B* **2014**, *118*, 6526–6530. [[CrossRef](#)] [[PubMed](#)]
190. Lazaridis, T.; Karplus, M. Thermodynamics of protein folding: A microscopic view. *Biophys. Chem.* **2003**, *100*, 367–395. [[CrossRef](#)] [[PubMed](#)]
191. Chong, S.-H.; Ham, S. Distinct Role of Hydration Water in Protein Misfolding and Aggregation Revealed by Fluctuating Thermodynamics Analysis. *Accounts Chem. Res.* **2015**, *48*, 956–965. [[CrossRef](#)] [[PubMed](#)]
192. Chong, S.H.; Ham, S. Examining a Thermodynamic Order Parameter of Protein Folding. *Sci. Rep.* **2018**, *8*, 7148. [[CrossRef](#)]
193. Fu, H.; Chen, H.; Wang, X.; Chai, H.; Shao, X.; Cai, W.; Chipot, C. Finding an Optimal Pathway on a Multidimensional Free-Energy Landscape. *J. Chem. Inf. Model.* **2020**, *60*, 5366–5374. [[CrossRef](#)]
194. Fu, H.; Shao, X.; Cai, W.; Chipot, C. Taming Rugged Free Energy Landscapes Using an Average Force. *Accounts Chem. Res.* **2019**, *52*, 3254–3264. [[CrossRef](#)]
195. Chandran, U.; Mehendale, N.; Tillu, G.; Patwardhan, B. Network Pharmacology of Ayurveda Formulation Triphala with Special Reference to Anti-Cancer Property. *Comb. Chem. High Throughput Screen.* **2015**, *18*, 846–854. [[CrossRef](#)] [[PubMed](#)]
196. Sakle, N.S.; More, S.A.; Mokale, S.N. A network pharmacology-based approach to explore potential targets of *Caesalpinia pulcherrima*: An updated prototype in drug discovery. *Sci. Rep.* **2020**, *10*, 17217. [[CrossRef](#)] [[PubMed](#)]
197. Fry, D.C. Targeting protein-protein interactions for drug discovery. *Methods Mol. Biol.* **2015**, *1278*, 93–106. [[PubMed](#)]
198. Fry, D.C. Protein-protein interactions as targets for small molecule drug discovery. *Biopolymers* **2006**, *84*, 535–552. [[CrossRef](#)]
199. Kanehisa, M.; Furumichi, M.; Tanabe, M.; Sato, Y.; Morishima, K. KEGG: New perspectives on genomes, pathways, diseases and drugs. *Nucleic Acids Res.* **2017**, *45*, D353–D361. [[CrossRef](#)]
200. Chen, L.; Zhang, Y.-H.; Lu, G.; Huang, T.; Cai, Y.-D. Analysis of cancer-related lncRNAs using gene ontology and KEGG pathways. *Artif. Intell. Med.* **2017**, *76*, 27–36. [[CrossRef](#)] [[PubMed](#)]